PRECISION MEASUREMENTS IN ^{20}F BETA DECAY

By

Maximilian Nathan Hughes

A DISSERTATION

Submitted to
Michigan State University
in partial fulfillment of the requirements
for the degree of

Physics – Doctor of Philosophy

2019

ABSTRACT

PRECISION MEASUREMENTS IN ^{20}F BETA DECAY

By

Maximilian Nathan Hughes

The beta decay of ^{20}F is an attractive low-energy probe for new physics. A parameter in beta decay highly sensitive to interactions beyond the standard model is the Fierz term. Since ^{20}F is a Gamow-Teller decay, the Fierz term corresponds to tensor couplings in weak interactions. A beta spectrum shape measurement was done to measure the Fierz term in ^{20}F. The analysis is not yet completed but a preliminary result is presented here. The current value of the Fierz term obtained is $0.0021 \pm 0.0051_{\text{stat}} \pm 0.0084_{\text{sys}}$.

In addition to the shape measurement, a half-life measurement was done. Previous measurements were inconsistent. The half-life was measured as $11.0011 \pm 0.0069_{\text{stat}} \pm 0.0030_{\text{sys}}$ s. This is the most precise measurement of the half-life of ^{20}F, and is 17 standard deviations away from the previously adopted value. This result has been confirmed by an additional measurement from another group using a different technique.

To my family

ACKNOWLEDGMENTS

I wouldn't have been able to do this work if it wasn't for the support of several people. First I'd like to thank Stan Paulauskas. He taught me a lot about research in my first year of grad school and helped me get my bearings. Next, I'd like to thank Xueying Huyan. She always answered any questions I had, especially those involving GEANT4. I'd like to thank Shloka Chandavar and Tom-Erik Haugen for giving me feedback during group meetings.

Thank you to Paul Voytas and Elizabeth George. Our phone meetings were a good check to make sure I wasn't doing things wrong. Thank you to Kei Minamisono for being my advisor during my first summer at the NSCL as an REU student. It was most of the reason I came to MSU. I'm grateful for all the people at the NSCL who made the experiment run.

Lastly, thank you to Oscar Naviliat-Cuncic. Your guidance was invaluable during my PhD. Hopefully we can finish the analysis.

TABLE OF CONTENTS

LIST OF TABLES . . . . . **viii**

LIST OF FIGURES . . . . . **ix**

Chapter 1 Introduction **1**
1.1 Beta Decay 2
1.1.1 Microscopic View of Beta Decay 3
1.1.2 Beta Energy Spectrum 3
1.2 Types of Precision Measurements in Beta Decay 5
1.2.1 Fierz Term 6
1.2.1.1 Previous Fierz Term Measurements 6
1.2.2 High Energy Probes of the Tensor Couplings 7

Chapter 2 Properties of ^{20}F Decay **9**
2.1 ^{20}F Decay Characteristics 9
2.2 Previous Measurements in ^{20}F Decay 10
2.2.1 Shape Measurements 12

Chapter 3 Theoretical Description of the Beta Energy Spectrum **16**
3.1 Experimental Inputs to Describe the Beta Spectrum 16
3.2 Phase Space Factor 18
3.3 Variables of the Correction Factors 18
3.4 Electromagnetic Corrections and Hadronic Corrections 19
3.4.1 Fermi Function 19
3.4.2 Radiative Correction 20
3.4.2.1 Inner Bremsstrahlung 22
3.4.3 Screening 23
3.4.3.1 Potentials Used in Screening Derivation 24
3.4.3.2 Screening Correction Formula 25
3.4.4 Finite Mass Correction 26
3.4.5 Finite Size Correction 26
3.4.6 Convolution of Lepton and Nucleon Wavefunctions 27
3.4.7 Hadronic Corrections 28
3.4.7.1 The Weak Magnetism 29
3.4.7.2 The Induced Tensor Form Factor 30
3.5 Summary 31

Chapter 4 Experimental Setup **33**
4.1 Experimental Technique 33
4.2 The ^{20}F Beam 34
4.2.1 Beam Size and Location 35

4.2.1.1 Verification of Implantation Depth . . . 37
4.3 Detector Configuration . . . 37
4.3.1 Detectors . . . 37
4.3.2 Powering the Detectors . . . 41
4.4 Experimental Conditions . . . 42

Chapter 5 Data Processing . . . 44
5.1 Data Acquisition . . . 44
5.1.1 Trapezoidal Filter Description . . . 45
5.1.2 Data Acquisition Software . . . 47
5.2 Data Taking and Processing . . . 48

Chapter 6 Half-life Measurement . . . 50
6.1 Motivation . . . 50
6.2 Half life Data Analysis . . . 51
6.2.1 Data Selection . . . 51
6.2.2 Cut Selection . . . 52
6.3 Systematic Effects . . . 58
6.3.1 Dead Time . . . 58
6.3.2 Pile-up Effects . . . 59
6.3.3 Background . . . 59
6.3.3.1 Simultaneous vs Separate Fitting . . . 60
6.3.3.2 Spectra Arguments . . . 61
6.3.4 Cut Sensitivity . . . 62
6.3.5 Oscillator Stability . . . 62
6.3.6 Binning and Fitting . . . 63
6.4 Result and Discussion . . . 63
6.5 Conclusion . . . 64

Chapter 7 GEANT4 Monte Carlo . . . 67
7.1 GEANT4 Inputs . . . 67
7.1.1 Detector Geometry . . . 67
7.1.2 Source Definition . . . 69
7.1.3 Primary Particle Definitions . . . 70
7.2 Particle Propagation . . . 71
7.3 Simulation Output . . . 71
7.4 Simulation Development . . . 72
7.4.1 Data Output Changes . . . 73

Chapter 8 Fitting Beta Spectrum . . . 75
8.1 Fitting Method . . . 75
8.2 Simulation Results Processing . . . 76
8.2.1 Detector Response . . . 78
8.2.1.1 Determining Detector Response . . . 79
8.2.2 Pile-up Modeling . . . 79

8.2.3 Fit Function 81
8.2.3.1 Fit Function Characterization 82
8.3 Experimental Data Processing 84
8.3.1 Background Subtraction 85
8.4 Beta Spectrum Fit Procedure 85
8.5 Systematic Uncertainties 86
8.5.1 Lower Beta Cut Sensitivity 87
8.5.1.1 The Offset 87
8.5.1.2 The Convolution 90
8.5.1.3 The Relative Normalization of the Beta-gamma Sum Spectrum 90
8.5.2 Upper Beta Cut Sensitivity 92
8.5.3 Summary of Systematic Uncertainties 92
8.6 Preliminary Results 95

Chapter 9 Conclusion 97
9.1 Outlook 97
9.1.1 Possible Improvements of the Technique 98

BIBLIOGRAPHY 100

LIST OF TABLES

Table 3.1: Variables used in the corrections. 19

Table 3.2: Coefficients for finite mass correction. 27

Table 3.3: Nuclear form factors. 28

Table 4.1: Detector voltages. 41

Table 5.1: DAQ cabling Scheme. 45

Table 5.2: Energy filter parameters. 47

Table 5.3: Trigger filter parameters. 47

Table 6.1: Settings for the PVT runs. 51

Table 6.2: Energy cuts for the gamma detectors. 52

Table 6.3: Energy cuts for the PVT detector. 54

Table 6.4: Half-life results. 63

Table 6.5: Systematics. 64

Table 8.1: The four histograms used for the fits. 75

Table 8.2: The values of the calibration parameters using the gamma sources. 77

Table 8.3: Pile-up model parameters compared to the energy filter parameters. . . . 81

Table 8.4: Systematic uncertainties due to simulation inputs. 93

Table 8.5: Systematic uncertainties due to fit inputs. 94

Table 8.6: Systematic uncertainties due to nuclear form factors. 95

LIST OF FIGURES

Figure 1.1: What beta$^-$ decay looks like microscopically. 3

Figure 1.2: The energy spectrum of the ultra-cold neutron measurement [4]. It was measured by the Ultra Cold Neutron A collaboration at Los Alamos National Lab. 7

Figure 2.1: The decay scheme of ^{20}F shown in context of the isospin triplet. The transition used the calculate b_{WM} is shown with the blue arrow. 10

Figure 2.2: A sample beta energy spectrum using a plastic scintillator detector [11]. The polarization of the decay was part of an experiment to put a limit on second class currents. This was measured at Tandem Accelerator Complex of the University of Tsukuba. 12

Figure 2.3: A sample beta energy spectrum using a spectrometer [12]. The goal of the experiment was a measurement of the spectrum shape. This was measured at Louvain University in Louvain-la-Neuve. 13

Figure 2.4: On the left there are simulated spectra of beta spectrum measured with a germanium detector [13]. The line is the original beta spectrum, and the crosses a simulated spectrum showing the back-scattering. On the right is the measured and fit ^{20}F beta spectrum. The residuals of the fit are shown above the beta spectrum. This experiment was to measure the shape of beta spectrum to measure the nuclear shape factor. The beta spectrum was measured at the Laboratory of Physics at the University of Montreal. 14

Figure 3.1: Electromagnetic and hadronic corrections for ^{20}F. Plotted are the Fermi function [18], the screening correction [19], the finite mass correction [20], the finite size correction [20], the radiative correction [21], the convolution of phase space correction [20], and the hadronic shape factor [22]. 20

Figure 3.2: Comparison of three different radiative corrections. The green line depends strongly on the detector geometry. 23

Figure 3.3: The numerical derivative of the ratios in 1/MeV. This is to check how sensitive the shape of the theoretical spectrum is to the uncertainty of the parameters extracted from experiment. These derivatives are an order of magnitude smaller than the 10^{-2}/MeV of the c_1 of the shape factor. . . 31

Figure 4.1: A sketch of the location of the detectors upstream of the implant detector. The detectors are not to scale. 35

Figure 4.2: The beam spot of the calibrated PPAC spectrum. The samples of the spectrum that were averaged together are shown in the black dots. The center of the fit is not shown. 36

Figure 4.3: The simulation is on the left. The data is on the right. All the fluorine is blocked after 14 mm of degrader. 38

Figure 4.4: A sketch of the PVT implant detector. The acrylic disk is seen along as PVT scintillator. The scale is in mm. 39

Figure 4.5: A sketch of the PVT implant detector set up. Notice that the PVT detector fills up the space between the gamma detectors. 39

Figure 4.6: A sketch of the CsI(Na) implant detector set up. The CsI(Na) detector is recessed 1 inch. 40

Figure 4.7: On the left the PVT set up can be seen. The rail the detector sits on and the optical fibers (the black cords) can be seen. On the right the CsI(Na) set up can be seen. In the center the implantation detector is seen. . . . 40

Figure 4.8: The modules used for the timing. "Disc" stands for discriminators. . . . 43

Figure 6.1: Previous measurements of the ^{20}F half-life. The labels correspond to: Mal [33], Gli [34], Yul [35], Wil [8], Alb [9], Gen [36], Min [37], Wan [38] and Ito [39]. 50

Figure 6.2: The light pulse as a function of time for set 1. The gain changes smoothly over time. This causes a large change in the half-life as the beta cuts are moved. 52

Figure 6.3: The y axis shows the gamma detector energy. The x axis is the implant detector energy. The ^{20}F coincidence region can be seen towards the top of the spectrum. The region at 511 keV can be seen closer to the bottom of the figure. 53

Figure 6.4: A beta spectrum built by applying the gamma cuts and time difference cuts. The beta cuts for the half-life analysis are shown as the red lines. The lower beta cut was selected to be above the 511 region. The upper beta cut was selected to include all the pile-up. 53

Figure 6.5: The red lines show the gamma cuts, which were chosen to reduce the effect of the rate dependent gain. On the left the spectrum is seen in a linear scale. On the right the spectrum is seen on a log scale. 54

Figure 6.6: The time difference between the up detector and the PVT implant detector. The tail on the right side of the large peak is due to pile-up. The time cuts are shown with a line. 55

Figure 6.7: A sketch of the pile-up events. A ^{20}F decay happens at time *t1*. The green electron is detected in the implant detector. The black arrow (the gamma ray) is not. Then, later at time *t2*, another ^{20}F decays. *t2* is within the pile-up window of *t1*. Both electrons energies pile-up and are added together. However, the time stamp recorded by the DAQ is still *t1*. The gamma ray from event *t2* can be detected in a gamma detector at time *t2*. This creates the uncorrelated event pedestal in the time difference graph. 56

Figure 6.8: The time difference spectrum zoomed out. This figure is built from with energy coincidences with energy cuts. 56

Figure 6.9: The decay spectrum from the up gamma detector is shown on the top graph. The red line is the exponential fit. The bottom graph shows the residuals from the fit. 58

Figure 6.10: Time difference vs the resulting half-life. The line is a quadratic fit which was extrapolated to zero. 60

Figure 6.11: The red lines show the results of the fits over the runs that were used. The additional half-lives shown are excluded to reasons discussed previously. 64

Figure 6.12: A scatter plot of previous values with this work added. The labels correspond to: Mal [33], Gli [34], Yul [35], Wil [8], Alb [9], Gen [36], Min [37], Wan [38] and Ito [39]. 65

Figure 7.1: A technical drawing of the CsI(Na) implant detector. 68

Figure 7.2: The detector geometry inside GEANT4. 69

Figure 7.3: Ratio of processing data two different ways. This is all the energy absorbed in the implant detector. 74

Figure 8.1: The shapes of the different histograms from the output of the GEANT4 simulation. The input beta spectrum is also plotted. The histograms are scaled to the same maximum. 77

Figure 8.2: A sample gamma spectrum showing the position of the gamma cuts used to build the beta spectrum. The blue lines show the cuts used to build the signal spectrum. The red lines show the cuts used to build the background spectrum. 78

Figure 8.3: The tuning of the pile-up. The input spectrum is in blue. The generated spectrum is in red. The red spectrum was generated from sampling the blue spectrum up to energy 1000 channels. These samples were put through the pile-up model. 80

Figure 8.4: A sample fit of the beta spectrum. The residuals of the fit are shown below the graph. The χ^2/NDF of this fit is 175.4/151. 86

Figure 8.5: Histograms of all the results from the fits. These graphs do not account for the uncertainties in each fit 86

Figure 8.6: For the standard model fit, there is a large dependence of the gain on the start of the fit. The offset here is 10.05. 88

Figure 8.7: This is Monte Carlo data. The curves were generated with an offset of 0 and fit with an offset of 15. A trend similar to that in the data is seen. . 88

Figure 8.8: How the slope of the G_{SM} vs LBC curve changes with offset. A slope of 0 corresponds to an offset of -5.1. 89

Figure 8.9: The dependence of the parameters to the start of the fit. The offset here is -5.1. Both gains are independent of the start of the fit. 89

Figure 8.10: A sample fitting of the gamma detectors over the Compton scattering range. 91

Figure 8.11: The ratio of the data to the fit function in the fits shown in figure 8.10. . 91

Figure 8.12: The effect of changing the upper beta cut. 93

Figure 8.13: This is the systematic uncertainty on b_{GT} due to the uncertainty of b_{WM}. It changes as a function of the lower beta cut. 95

Chapter 1

Introduction

The Standard Model of particle physics can be tested in several ways. For precision measurements, a careful measurement of a parameter thought to be zero within the Standard Model is done. If a non-zero result is found, new physics is discovered. One window for low energy precision measurements is beta decay. Low-energy measurements are not the only method to look for new physics.

The most direct way to look for new physics is to create and detect new particles. This is done with high energy experiments. The direct detection of new particles is very general and a powerful technique, as any avenue with a new particle can be probed. However, high enough energy is needed to create the particle. Precision measurements at high energies with colliders are often done as well.

Low energy precision measurements, on the other hand, are much more specialized. Precision measurements are sensitive to only certain channels of new physics. Care must be taken that the channel of physics is complementary to collider experiments. For nuclear physics searches, this can be done by looking at beta decay, which provides a sensitive probe to several avenues of new physics.

1.1 Beta Decay

Beta decay is one of the processes by which unstable nuclei transform. The general process is

$$ {}^{A}_{Z}P \rightarrow {}^{A}_{Z\pm1}D + e^{\mp} + \nu_e \tag{1.1} $$

with ${}^{A}_{Z}P$ being the parent nucleus, ${}^{A}_{Z\pm1}D$ being the daughter nucleus, $e^{\mp}$ is the outgoing electron or positron, and ν is an outgoing anti-neutrino or neutrino. This is an electron anti-neutrino in the case of beta^{-} decay, and an electron neutrino in the case of beta^{+} decay. A related process is electron capture, where a proton in the nucleus captures an inner electron and turns into a neutron.

The simplest type of nuclear beta decay is allowed beta decay. There are two types of allowed beta decay, which differ in angular momentum J and isospin T selection rules. These are called Fermi and Gamow-Teller transitions. For a Fermi transition, the change of the angular momentum J and the change of the isospin T are both zero. For a Gamow-Teller transition, the change in the angular moment J is 0 or ±1 and the change of the isospin T is 0 or ±1. However, a Gamow-Teller transition cannot cause a transition between two states of $J = 0$. Beta decays between two 0^{+} states are called super-allowed beta decays. There are also mixed allowed transitions, where both matrix elements of Fermi decay and Gamow-Teller decay contribute. In order to see what physics beyond the standard model beta decay measurements are sensitive to, a closer look at beta decay is needed.

1.1.1 Microscopic View of Beta Decay

At a microscopic level, the process of beta decay involves one of the quarks inside the nucleon emitting a W boson. This quark changes flavor, and the nucleon changes as well. The microscopic view of beta decay (for the beta$^-$ case) is shown in figure 1.1.

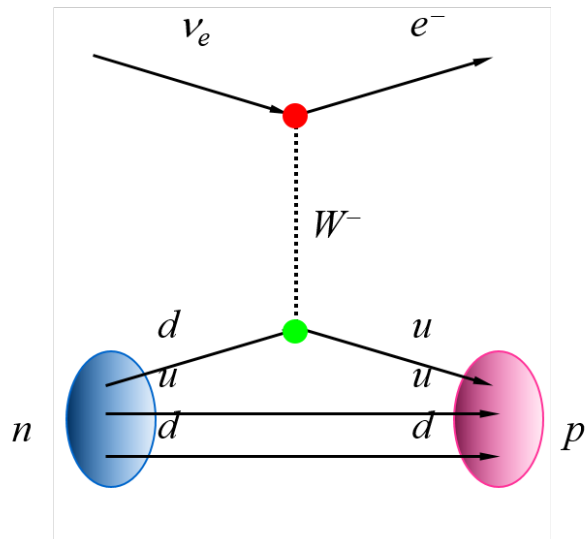

Figure 1.1: What beta$^-$ decay looks like microscopically.

A down quark in a neutron goes to an up quark. This process emits a W^- boson that decays into an electron and an electron anti-neutrino. Measurements of beta decay are complementary to high energy measurements of weak interactions. For this work, a nuclear level treatment of beta decay is done.

1.1.2 Beta Energy Spectrum

In order to determine the observables in beta decay, the energy spectrum must be written down. The spectrum is

$$\frac{d^2N}{dEd\Omega} = PS(E,\Omega) \times C(E,\Omega) \times W(E,\Omega) \tag{1.2}$$

with $d^2N/dEd\Omega$ the probability density of particles as a function of E, the energies of all outgoing particles, and Ω, the direction of all outgoing particles. The phase space, $PS(E,\Omega)$, and the corrections, $C(E,\Omega)$, will be discussed later in the thesis. The decay rate function, $W(E,\Omega)$, is [1]

$$W(E,\Omega) = \xi[1 + a\frac{\vec{p_e}\cdot\vec{p_\nu}}{E_eE_\nu} + b\frac{m_e}{E_e} + \frac{<\vec{J}>}{J}\cdot(A\frac{\vec{p_e}}{E_e} + B\frac{\vec{p_\nu}}{E_\nu} + D\frac{\vec{p_e}\times\vec{p_\nu}}{E_eE_\nu})] \tag{1.3}$$

where ξ is

$$\xi = |M_F|^2(|C_V|^2 + |C'_V|^2 + |C_S|^2 + |C'_S|^2) + |M_{GT}|^2(|C_A|^2 + |C'_A|^2 + |C_T|^2 + |C'_T|^2) \tag{1.4}$$

where M_F is the Fermi matrix element, M_{GT} the Gamow-teller matrix element, and the Cs are the nucleon level coupling constants. The subscripts of C indicate which object the coupling corresponds to. Here, A stands for axial vector, V stands for polar vector, S stands for scalar, and T stands for tensor. The C coefficients correspond to parity conserving interactions, and the C' coefficients correspond to parity non-conserving coefficients [2]. In equation 1.3, $<\vec{J}>$ is the average total angular momentum of the nucleus. The constants a, b, A, B, and D can be written in terms of the coupling constants. The $\vec{p_i}$ are the momenta of the particles, and the E_i the energies of those particles. The functional form of equation 1.3 informs the experimental design.

1.2 Types of Precision Measurements in Beta Decay

To measure the terms in equation 1.3, different types of experiments are needed. To extract a, both the direction of the neutrino momentum $\vec{p_e}$ and $\vec{p_\nu}$ are needed. The direction of electron momentum is measured directly. The direction of the neutrino momentum is calculated from the electron momentum and the momentum of the recoiling daughter nucleus. To measure A, B, or D, a polarized nucleus is needed. This points $< \vec{J} > /J$ in one direction, and then the corresponding momentum is measured. To measure A, for example, the direction of the outgoing electrons is measured. This direction corresponds to $AP\cos\theta$, where P is the polarization fraction and θ the direction of the electron momentum. Many more correlations exist involving the kinematic vectors.

For an unpolarized nucleus where only the energy of the electron is measured, the momenta are averaged over and all terms in equation 1.3 disappear except for b. This term is known as the Fierz term. There are two general kinds of unpolarized beta decay measurements. The first is where the differential energy spectrum is measured. There is a measurement of b over the entire range of values, and the entire $1/E$ dependence is probed. To do this measurement, the beta decay in question must be available enough in order to get enough statistics for a good spectrum. Other requirements for a spectrum shape measurement are described in the next chapter.

To extract the Fierz term electromagnetic and hardonic corrections are needed. For the shape measurements, the energy dependence of these corrections are important. Getting a better measurement of this term is one of the goals of this work.

1.2.1 Fierz Term

The Fierz term, b, in equation 1.3, can be rewritten in terms of effective couplings. This is

$$b\xi = \pm 2Re(|M_F|^2(C_S C_V^* + C_S' C_V'^*) + |M_{GT}|^2(C_T C_A^* + C_T' C_A'^*)) \tag{1.5}$$

where $Re()$ gives the real part of an imaginary number [1]. The positive sign corresponds to electron decay and the negative sign to positron decay.

This means, that in a pure Fermi decay, the Fierz term is sensitive to any non-standard scalar term, while in a pure Gamow-Teller decay, the Fierz term is sensitive to any non-standard Tensor term.

1.2.1.1 Previous Fierz Term Measurements

The Fierz term in Fermi decays have been extracted using super-allowed beta decays. The ft value was determined, which is the integral of the decay spectrum f times the partial half-life t. The partial half-life is the half-life times the branching ratio. This gives a value of b modulated by the average value of $1/E$. From the supperallowed beta decays, the result for the Fierz term is -0.0028 ± 0.0026 [3]. It was obtained with ft measurements of 14 different nuclei. The uncertainty is the statistical uncertainty of the fit after the ft values were corrected. However, this Fierz term is only sensitive to scalar couplings. To measure tensor couplings, a beta decay with a Gamow-Teller contribution is needed.

A spectrum shape measurement was done with ultra-cold neutrons [4]. The beta energy spectrum was measured using a magnetic spectrometer. The neutrons were confined in the center with a magnetic field, and allowed to decay. With the systematic effects, the final results of the Fierz term was $0.067 \pm 0.005_{\text{stat}}\ ^{+0.090}_{-0.061}\ _{\text{sys}}$. A sample beta spectrum is shown

in figure 1.2.

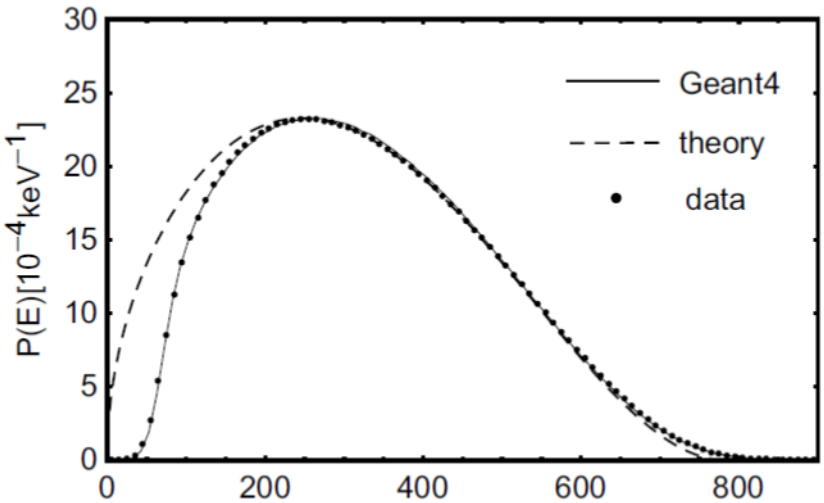

Figure 1.2: The energy spectrum of the ultra-cold neutron measurement [4]. It was measured by the Ultra Cold Neutron A collaboration at Los Alamos National Lab.

There is a large distortions at low energy. This distortion is due to threshold effects. Since the decay of a neutron is a mixed decay, this Fierz term is sensitive to both the tensor couplings and the scalar couplings.

1.2.2 High Energy Probes of the Tensor Couplings

There are probes sensitive to the same physics as in Fierz term done with high energy techniques [5]. The precision of these measurements is important to keep in mind, as this is the precision goal of the beta decay measurement. Several high-energy channels are used, and the coupling constants are directly measured. To compare the results of the channels to a precision beta decay measurement, the Fierz terms needs to be rewritten. In the case of a pure Gamow-Teller transition, the Fierz term in equation 1.5 can be re-written as

$$b_{GT} = \pm 2\sqrt{1-\alpha^2 Z^2} Re\left(\frac{C_T + C'_T}{C_A + C'_A}\right) \tag{1.6}$$

where α is the fine structure constant and Z the atomic number of the daughter nucleus. In terms of the quark level coupling constants, this can be rewritten as [5]

$$b_{GT} = \pm 2\sqrt{1-\alpha^2 Z^2} Re\left(\frac{8 g_T \epsilon_T}{2 g_A}\right) \tag{1.7}$$

with g_T being the tensor charge, ϵ_T the tensor coupling and g_A the axial vector charge. This is assuming the only physics beyond the standard model is in ϵ_T. The value of g_T is 0.987(55) and g_A is 1.278(33) [5]. This means, for ^{20}F, the value to b_{GT} in terms of ϵ_T is given by

$$b_{GT} = 6.2 \times Re(\epsilon_T) \tag{1.8}$$

This can be used to describe the ultimate sensitivity needed.

For the high energy probes, the Large Hadron Collider collides two protons and looks at the output. The experimental signature for the LHC is missing transverse energy. The energy of the output particles is compared to that of the standard model background, and the difference recorded. To probe the same physics as beta decay, one or more of the outgoing particles are electrons or positrons. For events with one electron and other particles, the constraint is $|\epsilon_T| < 1.3 \times 10^{-3}$ [6]. Looking at neutral currents, where the output particles include an electron and a positron, gives stronger constraints. There, the constraint is $|\epsilon_T| < 0.6 \times 10^{-3}$ [7]. To be competitive with the stronger constraint from high energy experiments, the Fierz term b_{GT} should be measured to better than 3.7×10^{-3}, assuming that ϵ_T is real. In order to achieve such a sensitivity, the technique used was a shape measurement.

Chapter 2

Properties of ^{20}F Decay

For a potential beta energy spectrum shape measurement, several criteria for a nucleus are needed. The first is that the nucleus and the decay mode must be available in sufficient quantities that a proper decay spectrum shape can be measured. This means that the nucleus needs to be relatively close to stability. The decay mode needs to be clean. If there are several competing decay modes of similar strength, the shape of the beta decay spectrum gets complicated. The same thing happens if there are several gamma rays in the decay. Having one gamma ray is useful, as a coincidence measurement can be used to exclude much of any background in the measurement. An allowed Gamow-Teller transition gives sensitivity to tensor couplings. A nucleus that fulfills these criteria is ^{20}F.

2.1 ^{20}F Decay Characteristics

The decay scheme is given in figure 2.1. As seen in the figure, ^{20}F decays 99.99% of the time to the first excited state of ^{20}Ne. This decay is very clean, as there are very few contaminants from other decay branches. The 2^+ state seen in the decay scheme is not the isobaric analogue state to the ground state of ^{20}F. That state is much higher in energy. The beta decay therefore has an isospin change of 1. This means that the allowed Fermi matrix element is zero, and the decay is an allowed Gamow-Teller transition. The forbidden transitions only contribute to higher order. The half-life of ^{20}F is about 11 seconds. This

means waiting for the ^{20}F to decay will take less than a minute to get good statistics.

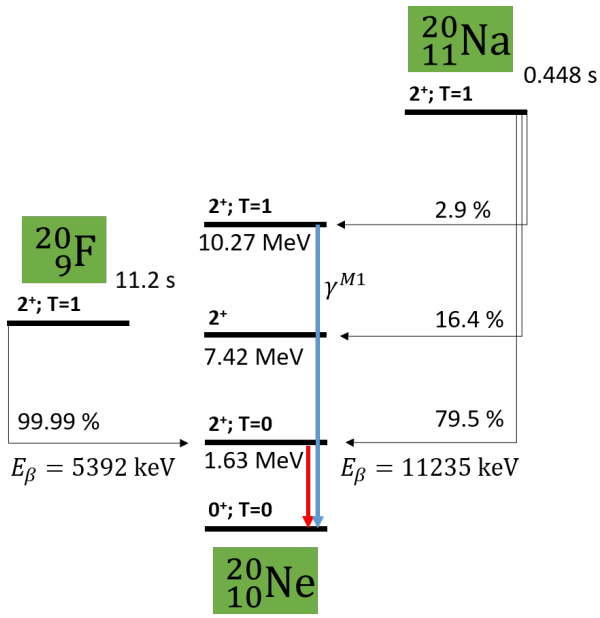

Figure 2.1: The decay scheme of ^{20}F shown in context of the isospin triplet. The transition used the calculate b_{WM} is shown with the blue arrow.

The 1.6 MeV gamma ray in the transition, the red arrow in figure 2.1 allows for a coincidence measurement to take place. One gamma ray does not distort the spectrum much. ^{20}F is relatively close to stability, so it can be made in sufficient quantities to get high statistics.

2.2 Previous Measurements in ^{20}F Decay

Some of the earliest measurements of ^{20}F were ft value measurements [8] [9]. The half-lives were measured with a plastic scintillator in both cases. These ft values were compared to the mirror nucleus ^{20}Na in order to search for second class currents in beta decay. Second class currents have different properties under G-parity than first class currents [10].

Another, more recent measurement whose goal was putting limits on second class currents was done with with a polarized ^{20}F and ^{20}Na beam [11]. The technique was an alignment

measurement over different energies. The ^{20}F was made with a polarized deuteron beam impinging on a ^{19}F target. The direction of the outgoing electron was measured and recorded. The angular distribution was measured using the beta-nuclear magnetic resonance (NMR) technique. Plastic scintillators at the end of magnets were used to measure the direction of the electrons. The correlations were corrected for and plotted vs energy. The outcome of that analysis was a measurement of the various form factors that correct the beta decay spectrum shape. Specifically, the second-class current induced tensor term was measured. The resulting ^{20}F energy spectrum is shown in figure 2.2. In this spectrum, there are several background contributions. Since this measurement was an asymmetry measurement, the influence of the backgrounds is reduced. Different polarizations were used to eliminate systematic effects. Double ratios were taken to account for difference in solid angle and detector efficiency. The threshold was taken to be 2 MeV, as below that energy, the spectrum is distorted.

There are several important systematic effects in this measurement. The two largest have to do with corrections for the solid angle and corrections for the 1.634 MeV gamma ray. The corrections for the solid angle have to do with estimates of the scattering of the electrons. This happens at the implantation target, and can happen on the walls of the spectrometer. To counteract this effect, a veto detector was included in the detector set up. This veto detector was situated near the walls of the magnet, so any scattering off of the magnet could be vetoed. The other large systematic effect has to do with gamma rays. Since the ^{20}F is polarized, the direction of the emitted gamma rays is anisotropic. The gamma rays contribute and pile-up with the detected beta spectrum in different ways. This has to be corrected for with the detector response. With all these effects, the second-class current induced tensor form factor was measured as 0.18 ± 0.48, consistent with zero.

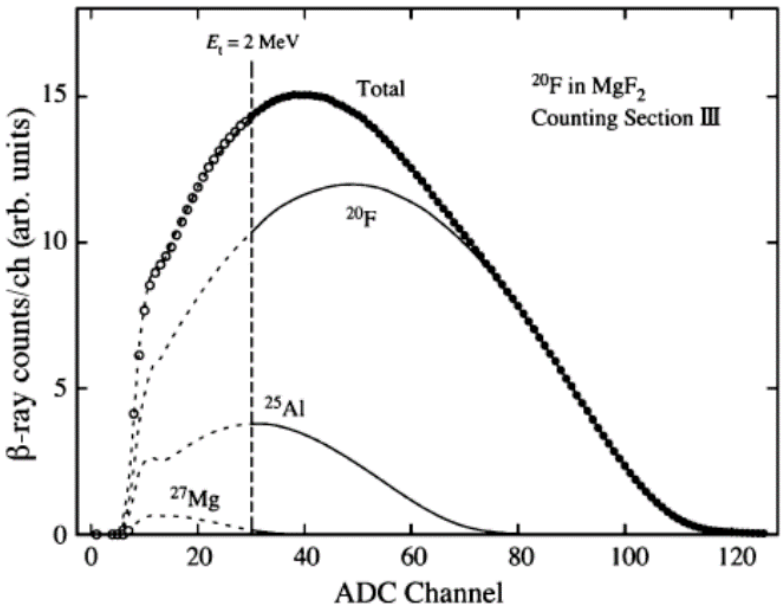

Figure 2.2: A sample beta energy spectrum using a plastic scintillator detector [11]. The polarization of the decay was part of an experiment to put a limit on second class currents. This was measured at Tandem Accelerator Complex of the University of Tsukuba.

2.2.1 Shape Measurements

Several direct shape measurements have been made in ^{20}F. Two measurements with different systematic effects will be discussed. Both of them looked for the linear term in the hardonic correction to the beta decay spectrum shape.

A measurement of the ^{20}F spectrum shape was done with a spectrometer [12]. This shape factor will be described further in a later chapter. The ultimate goal was to test the conserved vector current (CVC) hypothesis. ^{20}F was created with a deuteron beam on a ^{19}F target. The target was ^{6}LiF on a carbon foil. After the target was bombarded, and the ^{20}F created, the outgoing electron went through the foil and into the spectrometer. The spectrometer was tuned to accept a certain energy of electrons. Then, data on the decay of ^{20}F at different electron energies were collected. A sample energy spectrum is shown in figure 2.3.

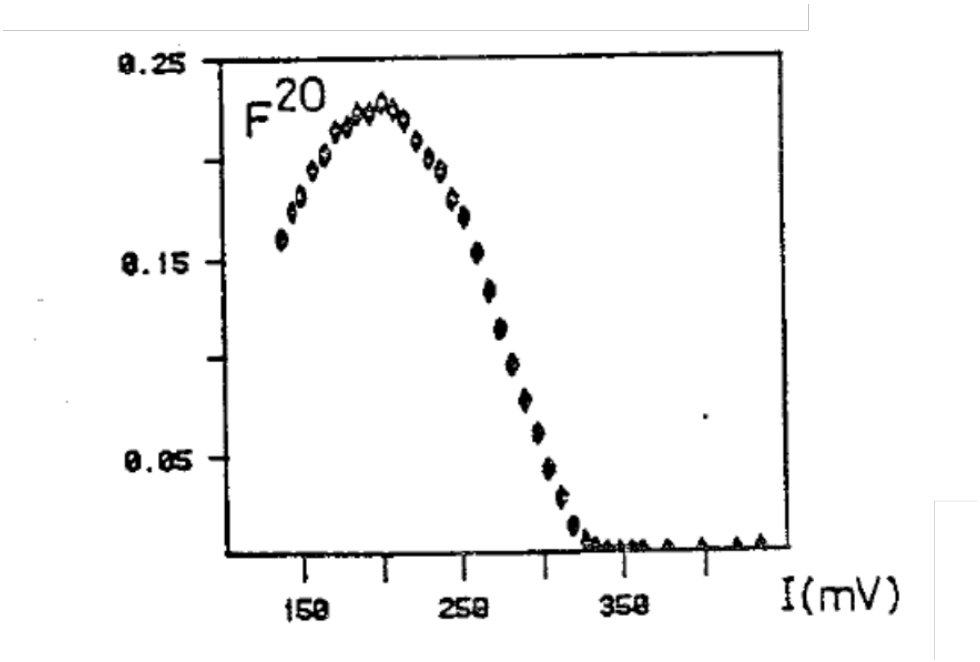

Figure 2.3: A sample beta energy spectrum using a spectrometer [12]. The goal of the experiment was a measurement of the spectrum shape. This was measured at Louvain University in Louvain-la-Neuve.

An important consideration is the normalization of each point. For each spectrometer setting, the amount of measurement time, the acceptance of the spectrometer, and the source activity have to be accounted for. To help with the normalization, a beta telescope near the target was used. This measures the activity of the source, and takes into account the degradation of the target. However, there are still issues with adjusting for the efficiency of the beta telescope. This efficiency changes as the spectrometer's field is changed. The location of the telescope was optimized to minimize this effect. Another way of normalization was to continuously adjust the spectrometer field so that a the entire energy range is sampled over each measurement cycle. The issue there is that changing the magnetic fields induces currents that are hard to correct for. In that measurement, adjusting the spectrometer field was used as a benchmark for the beta telescope normalization method.

An issue with this measurement is that the shape factor is not just the linear term. The

shape factor depend on the other nuclear form factors and are not independent. The other terms were calculated and fixed. Ultimately the resulting measurement of the linear term was 0.0057 ± 0.0004 /m_e, where m_e is the mass of the electron.

A different shape measurement used a single detector, which took care of the normalization automatically. A shape measurement of ^{20}F was made with a spectrometer and a high purity germanium detector [13]. The linear term in the shape factor was measured just like in the previous measurement. The magnetic field was used to enhance the solid angle for the electrons compared to the gamma rays. The ^{20}F was made with a deuteron beam on a natural LiF target. An implant and decay cycle was used to measure the beta decay spectrum. A simulated and a data beta spectrum are shown in figure 2.4.

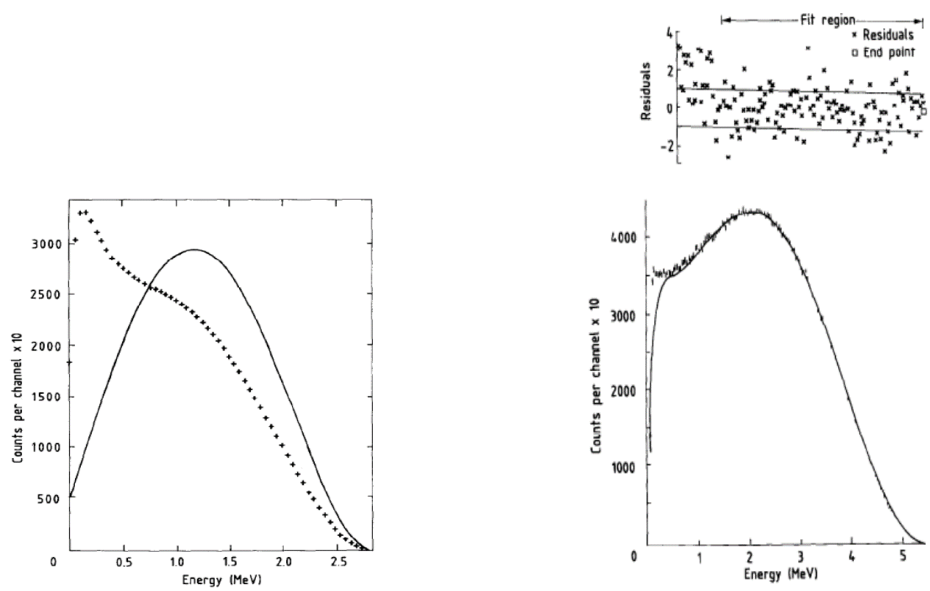

Figure 2.4: On the left there are simulated spectra of beta spectrum measured with a germanium detector [13]. The line is the original beta spectrum, and the crosses a simulated spectrum showing the back-scattering. On the right is the measured and fit ^{20}F beta spectrum. The residuals of the fit are shown above the beta spectrum. This experiment was to measure the shape of beta spectrum to measure the nuclear shape factor. The beta spectrum was measured at the Laboratory of Physics at the University of Montreal.

As seen from figure 2.4, there is a large distortion at low energies. This is due to back-

scattering inside the germanium detector. What happens is that electrons enter the detector, deposit some of their energy, and bounce back out. This causes events that should be at higher energies to be instead read at very low energies.

Another issue for this measurement was that energy calibration was non-linear. Below 1.5 MeV, there was a non-linearity which caused a distortion down to 35 keV. This all had to be accounted for and contributed to the uncertainty. The resulting energy spectrum and fit is shown on the right in figure 2.4.

The beta spectrum is greatly distorted. The effective shape measurement analysis was started at 1.5 MeV. For this measurement there were several systematic effects. The largest systematic uncertainty is due to what paper refers to as "peak fraction." This is part of the model of how the detector responds to electrons, which is known as the response function. Specifically, the "peak fraction" is the ratio of the integral of the full energy peak in the response function to the total integral of the response function. This experiment used many different sources to get the calibration and the response function. They also had to take the bremsstrahlung of the electrons into account. The systematic uncertainties were larger than the statistical uncertainties in this measurement.

Much like the spectrometer measurement, the other terms of the shape factor were fixed. Here however the other terms were calculated as a systematic error. It was found that the E^2 term had more of an effect in the measurement than the $1/E$ term. Ultimately, the measured linear term was 0.0060 ± 0.0018 /m$_e$, which is consistent with the CVC hypothesis.

The present work is also a spectrum shape measurement, much like the two cited above. The ultimate goal is however a determination of the Fierz term. In order to get the Fierz term, the beta energy spectrum must be described precisely.

Chapter 3

Theoretical Description of the Beta Energy Spectrum

To obtain a measure of the Fierz term, the beta energy spectrum must be accurately described. The description of the beta energy spectrum is written as a series of corrections multiplying the main phase space factor. Through out this chapter, $\hbar = c = 1$.

The beta energy spectrum shape can be broken up in three different factors. The three terms are written out as

$$\frac{dN}{dE} = PS(E) \times C(E) \times (1 + b_{GT}\frac{m_e}{E}) \tag{3.1}$$

$PS(E)$ is the phase space of the electron, $C(E)$ are all the hadronic and electromagnetic corrections multiplied together, and b_{GT} the Fierz term. This chapter will describe all that goes into the determining the beta energy spectrum.

3.1 Experimental Inputs to Describe the Beta Spectrum

The corrections depend on several parameters of the decay. Some of them are just numbers, such as the atomic number of the daughter or mother nucleus or the mass number of the

system. However, there are two important parameters that are extracted from experimental measurements and therefore have some uncertainty. One is the Q-value of the decay, which is defined as

$$Q = m_{^{20}F} - (m_{^{20}Ne} + E_{level}) \tag{3.2}$$

where $m_{^{20}F}$ is the nuclear mass of ^{20}F, $m_{^{20}Ne}$ is the nuclear mass of ^{20}Ne, and E_{level} is the energy of the 1.6 MeV nuclear state in ^{20}Ne. The tabulated masses for these nuclei are the atomic masses, M, which differ from the nuclear masses by the electron mass and the binding energy of the electrons. The electron masses are subtracted off, since the binding energy of the electrons is insignificant. For ^{20}F, $M_{20Ne} = 19.9924401762(17)$ amu, $M_{20F} = 19.999981252(31)$ amu [14] , and $E_{level} = 1.633674(15)$ MeV [15] .

This mass difference is not quite the maximum electron energy. To get to the maximum electron energy, E_0, the energy of the recoiling nucleus has to be taken into account. The formula is [16]

$$E_0 = Q\left(\frac{1 + \frac{m_e^2}{2M_{ave}Q}}{1 + \frac{Q}{2M_{ave}}}\right) \tag{3.3}$$

with m_e is the electron mass and M_{ave} is the average nuclear mass.

The other parameter is the charge radius of the daughter nucleus. There are several ways to calculate the charge radius. In this work, the charge radius was taken from the measured root mean square (RMS) charge radius and converted to the charge radius R. It was assumed that the ^{20}Ne nucleus was a sphere. From this, the radius was calculated using

$$R = \sqrt{\frac{5}{3}} r_{rms} \tag{3.4}$$

where r_{rms} is the root mean square charge radius, and R the charge radius. For this work, $r_{rms} = 3.0055(21)$ fm [17].

3.2 Phase Space Factor

The main part of the beta energy spectrum is the phase space factor. It is

$$\frac{dN}{dE} = C \times p_e W (W_0 - W)^2 \tag{3.5}$$

where dN/dE is the spectrum of electrons emitted as a function of energy, C is a constant, p_e is the electron momentum, W the total electron energy divided by m_e, and W_0 the maximum electron energy divided by m_e. This is derived from the density of states of the particle when the neutrino degrees of freedom are integrated over. The constant has factors that come from that integration.

3.3 Variables of the Correction Factors

For the rest of the discussion of the corrections to the energy spectrum, everything is given without units. These corrections are largely electromagnetic in origin. All of the energies are divided by the electron mass. For this work, $m_e = 0.510998928$ MeV. The other important variables are shown in table 3.1.

Table 3.1: Variables used in the corrections.

Variable	Description	Equation or Value
A	Mass number	20
Z	Atomic number of daughter	10
α	Fine structure constant	1/137.0359
R	Charge radius of daughter	3.8801 fm [17]
W	Total energy of the electron	E/m_e
p	Electron momentum	$\sqrt{W^2-1}$
W_0	Maximum electron energy	5.900864 (82) MeV
M_{ave}	Average nuclear mass	18621.497033 (40) MeV
$\gamma = \sqrt{1-(\alpha Z)^2}$	γ factor	0.9973

3.4 Electromagnetic Corrections and Hadronic Corrections

A graph of the various electromagnetic corrections is shown in figure 3.1, along with the hadronic shape factor.

3.4.1 Fermi Function

In absolute value, the largest correction is the Fermi function. This accounts for the interaction of the charge of the outgoing electron and the charge of the nucleus. It is calculated by taking the Dirac equation wave functions and assuming the nucleus is a point charge of Ze. The Dirac wave functions are taken down to a nuclear radius R. This is since the wave functions diverge [18]. The Fermi function is

$$F(Z,W) = 2\frac{\gamma+1}{\Gamma(2\gamma+1)^2}(2pR)^{2(\gamma-1)}e^{\frac{\pi\alpha ZW}{p}}\|\Gamma(\gamma+i\frac{\alpha ZW}{p})\|^2 \tag{3.6}$$

While this is the largest correction, it is the most understood one. There is no change of shape due the uncertainty in R because it alters as a factor the functional form of the Fermi

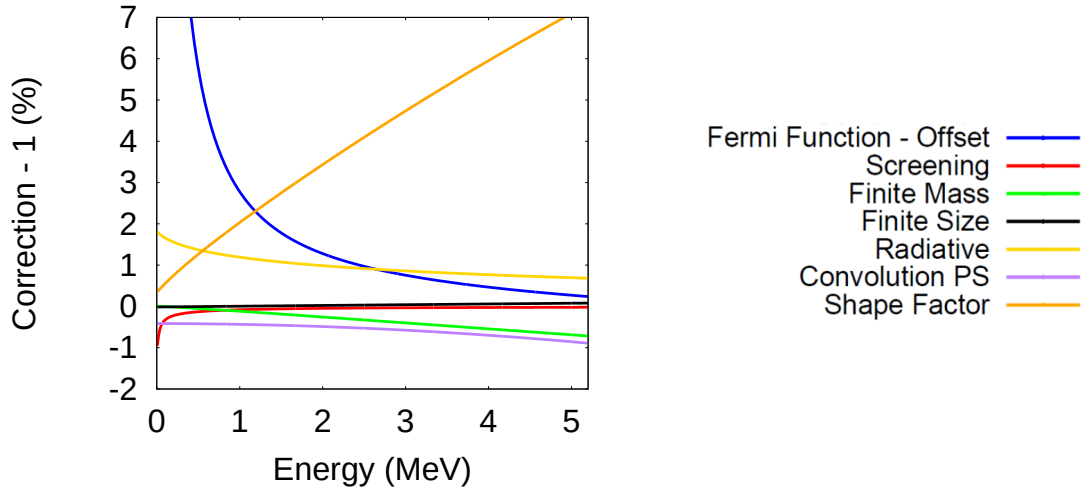

Figure 3.1: Electromagnetic and hadronic corrections for ^{20}F. Plotted are the Fermi function [18], the screening correction [19], the finite mass correction [20], the finite size correction [20], the radiative correction [21], the convolution of phase space correction [20], and the hadronic shape factor [22].

function.

3.4.2 Radiative Correction

The radiative correction is the next largest electromagnetic correction. For this measurement, the correction is only needed to first order, which is on order α. The correction is a quantum electrodynamics correction that stems from photons emitted from the beta particle. This photon can be absorbed by the nucleus of the daughter, which makes it a virtual photon. The photon can also be a real photon that propagates off to infinity. The real photons are known as inner bremsstrahlung.

There are different descriptions of the radiative correction. The standard is by Sirlin [23] and is

$$
\begin{aligned}
R(W,W_0) =& 1 + \frac{\alpha}{2\pi}[3\ln(M_p) - \frac{3}{4} + 4(\frac{\operatorname{arctanh}(\beta)}{\beta} - 1) \times (\frac{W_0 - W}{3W} - \frac{3}{2} + \ln(2(W_0 - W))) \\
&+ \frac{4}{\beta} L\left(\frac{2\beta}{1+\beta}\right) + \frac{\operatorname{arctanh}(\beta)}{\beta} \times (2 \times (1+\beta^2) + \frac{(W_0 - W)^2}{6W^2} - 4\operatorname{arctanh}(\beta))]
\end{aligned}
\tag{3.7}
$$

with $\beta = \frac{p}{W}$, M_p the proton mass divided by the electron mass, and $L(\frac{2\beta}{1+\beta})$ referring to the Spence function, which is [24]

$$
L(x) = \int_0^x \frac{\ln(1-t)}{t} dt \tag{3.8}
$$

The Sirlin formula assumes that the inner bremsstrahlung photons are not detected at all. This is mostly true if the source of the beta decay is outside of a detector. However, if the source is implanted inside of the detector, such as it is in this experiment, some of the inner bremsstrahlung is absorbed.

If all of the inner bremsstrahlung is absorbed, a different form of the first order radiative correction is needed. There are many equivalent forms of this, but the one that was used for this experiment was by Fayans [21]. The form of this radiative correction is

$$
\begin{aligned}
R(W,W_0) =& 1 + \frac{\alpha}{\pi}[(\frac{2}{\beta}\ln\left(\frac{2\beta}{1+\beta}\right) + \frac{7}{8\beta} + \frac{3\beta}{8})\ln\left(\frac{1+\beta}{1-\beta}\right) \\
&- 2\ln\left(\frac{4\beta^2}{1-\beta^2}\right) + \frac{4}{\beta}L\left(\frac{2\beta}{1+\beta}\right) + \frac{23}{8} + \frac{3}{2}\ln(M_p)]
\end{aligned}
\tag{3.9}
$$

The amount of inner bremsstrahlung absorbed depends obviously on the geometry. Since the detector is small enough not to absorb all of the inner bremsstrahlung, a more careful treatment of the radiative correction is needed.

3.4.2.1 Inner Bremsstrahlung

To first order, the energy spectrum of the inner bremsstrahlung photons is independent of Z. This is exactly like the two radiative corrections shown in equations 3.7 and 3.9. The spectrum is written as [25]

$$\Phi(k, W_e) = \frac{\alpha p}{\pi p_e k}[\frac{W_e^2 + W^2}{W_e p} log(W + p) - 2] \tag{3.10}$$

where $\Phi(k, W_e)$ is the probability density of emitting a photon of energy k from an electron of initial energy W_e. This equation was derived using outgoing waves from the Dirac equation in polar coordinates. This was calculated with the first order Born approximation. This means that at low energies, equation 3.10 is inaccurate. That can be seen, as the equation diverges as k goes to zero. If more orders of the approximation are added, this divergence can be controlled. These higher orders would correspond to emitting multiple photons. Each of these orders would have a probability reduced by a factor of α compared to equation 3.10. The higher orders would be less significant, except at low energies, where the probability density diverges. This would make the probability of emitting no photons finite. However, another possibility is to add a cutoff. As long as the cutoff is high enough to be in the region where the first order Born approximation is valid, but low enough not to cut out gamma rays that are not fully absorbed, equation 3.10 is valid. The cutoff used was 50 keV. This cutoff was checked using Monte Carlo simulation, and is within the region where the detector and the source geometry absorbs all gamma rays.

To quantify the effect of the inner bremsstrahlung, a GEANT4 simulation was used. Electrons were generated using the phase space and the radiative correction in equation 3.9. Then, for each electron, equation 3.10 was sampled and a photon generated. No other

physics process was looked at in this simulation. The ratio consisting of the energy absorbed over the initial energy was the output of the simulation. That ratio is the effective efficiency of absorbing the inner bremsstrahlung photons. Multiplying that ratio by equation 3.9 gives the effective radiative correction. The comparison of all three radiative corrections is shown in figure 3.2.

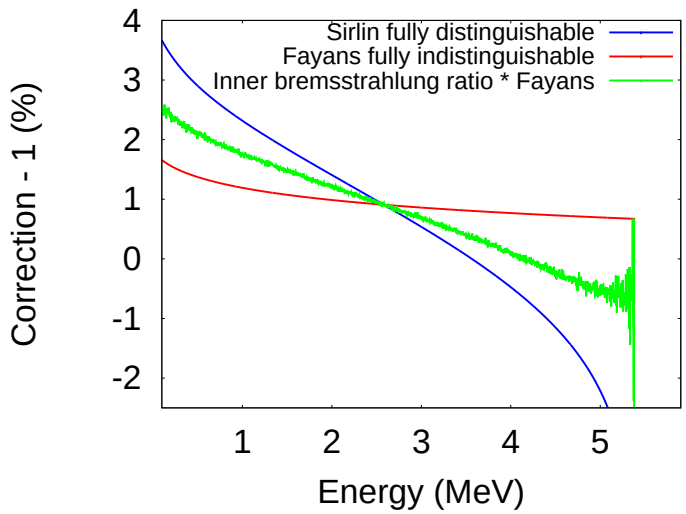

Figure 3.2: Comparison of three different radiative corrections. The green line depends strongly on the detector geometry.

The effect of the inner bremsstrahlung for a finite detector is to put the radiative correction halfway between the Sirlin and the Fayans formulas.

3.4.3 Screening

The screening correction is the next largest electromagnetic correction. This is a correction to the Fermi function. It corresponds to the screening of the nuclear charge due to the electron cloud of the atom. The strongest effect of the screening correction is at low electron energies and for large atomic numbers.

3.4.3.1 Potentials Used in Screening Derivation

To calculate this correction, the Coulomb potential used to calculate the Fermi function is replaced with a Hulthén potential. This potential is

$$V(r) = -\frac{\alpha Z \beta}{e^{\beta r} - 1} \tag{3.11}$$

where r is the distance away from the center and β is a parameter characterizing the diffuseness of the electron cloud. The ratio of this new Fermi function to the old Fermi function is the screening correction which multiplies the phase space.

The screening correction is negligible except near the origin, while near the origin, equation 3.11 behaves as

$$V(r) = -\frac{\alpha Z}{r} + \frac{1}{2}\alpha Z \beta \tag{3.12}$$

and β is given by [19]

$$\beta = 2C(Z)\alpha Z^{1/3} m_e \tag{3.13}$$

Here, the Z is number the electrons of the daughter atom because the assumption is that beta decay is occurring from neutral atoms. The only unknown is $C(Z)$.

To find the value of $C(Z)$, a comparison is needed. In another method of describing screening, the potential is described as a series of exponentials. This is written as [26]

$$V(r) = -\frac{\alpha Z}{r} \sum_n c_n e^{-b_n x} \tag{3.14}$$

where b_n and c_n are constants. The sum of all the c_n adds up to one. The value of x is [26]

$$x = 1.13\alpha Z^{1/3} r m_e \tag{3.15}$$

When equation 3.14 is expanded near the origin and x is written explicitly, the result is

$$V(r) = -\frac{\alpha Z}{r} + \frac{1}{2}\alpha Z \times 2(1.13\sum_n b_n c_n)\alpha Z^{1/3} m_e \tag{3.16}$$

By comparing equations 3.12 and 3.13 with 3.16, the result obtained is

$$C(Z) = 1.13\sum_n c_n b_n \tag{3.17}$$

There is only one term in ^{20}F. The parameters in equation 3.17 are $c_1 = 1$ and $b_1 = 0.907$ [26].

3.4.3.2 Screening Correction Formula

From equation 3.17, the factor $C(Z)$ in equation 3.13 is evaluated $0.907 \times 1.13 = 1.02491$. Equation 3.12 can then be used to calculate the screening correction. The result is [19]

$$Q(Z,W) = X(\frac{W'}{W})\left|\frac{\Gamma(\gamma+iy')}{\Gamma(\gamma+iy)}\right|^2 \left|\frac{\Gamma(\gamma+2i\frac{p'}{\beta})}{\Gamma(\gamma+2i\frac{p}{\beta})}\right|^2 e^{-\pi y}(\frac{2p}{\beta})^{2(1-\gamma)} \tag{3.18}$$

with $y = \frac{\alpha Z W}{p}$, $y' = \frac{\alpha Z W'}{p'}$,$\gamma$ is in table 3.1, $W' = W - \frac{1}{2}\alpha Z\beta$, and $p' = \frac{1}{2}p + \frac{1}{2}\sqrt{p^2 - 2\alpha Z W'\beta}$. $X(\frac{W'}{W})$ is

$$X = \frac{1 + \frac{W'+\gamma m_e}{8W'}(\frac{\beta}{p})^2 + \frac{1}{2}\gamma^2[1 + (1 - \frac{\alpha Z\beta}{(W+m_e)})^{1/2}]^{-2}[\frac{W-m_e}{W'}](\frac{\beta}{p})^2[1 - \frac{1-\gamma}{8\gamma}(\frac{\beta}{p})^2]}{(1 + \frac{\beta}{4p}^2)} \tag{3.19}$$

The factor X in equation 3.19 is very close to 1. This correction matters mostly at low energy, and is very flat above 100 keV.

3.4.4 Finite Mass Correction

The finite mass correction accounts for the recoil motion of the ^{20}Ne nucleus. The form of finite mass corrections is given as [20]

$$R(W, W_0, m_{^{20}Ne}) = 1 + r_0 + \frac{r_1}{W} + r_2 W + r_3 W^2 \tag{3.20}$$

The forms of the r_i depend on if the decay is a vector decay or an axial decay. This is due to angular momentum conservation. Since ^{20}F is an axial decay, the finite mass correction coefficients are

$$\begin{aligned}
r_0 &= -\frac{2W_0}{m_{^{20}Ne}} - \frac{W_0^2}{6(m_{^{20}Ne})^2} - \frac{77}{18(m_{^{20}Ne})^2} \\
r_1 &= -\frac{2}{3m_{^{20}Ne}} + \frac{7W_0}{9(m_{^{20}Ne})^2} \\
r_2 &= \frac{10}{3m_{^{20}Ne}} - \frac{28W_0}{9(m_{^{20}Ne})^2} \\
r_3 &= \frac{88}{9m_{^{20}Ne}}
\end{aligned} \tag{3.21}$$

This correction is different from the hadronic shape factor described later.

3.4.5 Finite Size Correction

The finite size correction originates from treating the nucleus as a uniformly charged sphere instead of a point particle. This sphere has a radius of R, as shown in equation 3.4. The

form of the finite size correction is [20]

$$L_0(Z,W) = 1 + \frac{13(\alpha Z)^2}{60} - \alpha ZWR\frac{41-26\gamma}{15(2\gamma-1)} - \alpha ZR\gamma\frac{17-2\gamma}{30W(2\gamma-1)} \\ +a_{-1}\frac{R}{W} + \sum_{n=0}^{5} a_n(WR)^n + 0.41(R-0.0164)(aZ)^{4.5} \tag{3.22}$$

Where the a_n coefficients are parameterized by

$$a_n = \sum_{x=1}^{6} b_x^n(\alpha Z)^x \tag{3.23}$$

The b_x coefficients are numbers shown in table 3.2.

Table 3.2: Coefficients for finite mass correction.

	b_1^n	b_2^n	b_3^n	b_4^n	b_5^n	b_6^n
a_{-1}	0.115	-1.8123	8.2498	-11.223	-14.854	32.086
a_0	-0.00062	0.007165	0.01841	-0.053736	1.12691	-1.5467
a_1	0.02482	-0.05975	4.84199	-15.3374	23.9774	-12.6534
a_2	-0.14038	3.64953	-38.8143	172.1368	-346.708	288.7873
a_3	0.008152	-1.15664	49.9663	-273.711	657.6292	-603.7033
a_4	1.2145	-23.9931	149.9718	-471.2985	662.1909	-305.6804
a_5	-1.5632	33.4192	-255.1333	938.5297	-1641.2845	1095.358

3.4.6 Convolution of Lepton and Nucleon Wavefunctions

This is the last of the relevant electromagnetic corrections. In figure 3.1, the name given is, "convolution PS." This correction $C(Z,W)$ accounts for the interaction of the lepton and nucleon wavefunctions. The radial part of the nucleon wavefunctions is modeled as a rectangle with width R. Much like the finite size and mass corrections, this correction depends on the type of β decay. Since the decay of interest is an axial vector decay, the form

of this correction is

$$C(Z,W) = 1 + C_0 + C_1 W + C_2 W^2 \tag{3.24}$$

where the C_i coefficients are defined as [20]

$$\begin{aligned} C_0 &= -\frac{-233(\alpha Z)^2}{630} - \frac{(W_0 R)^2}{5} + \frac{2\alpha Z R W_0}{35} \\ C_1 &= -\frac{21\alpha Z R}{35} + \frac{4W_0 R^2}{9} \\ C_2 &= -\frac{4R^2}{9} \end{aligned} \tag{3.25}$$

This correction depends on both the maximum energy of the outgoing electron and the charge radius. The contribution from this correction to the shape is minimal.

3.4.7 Hadronic Corrections

Nuclear form factors are one of the largest corrections to the beta spectrum. There are four relevant form factors that come together into a correction called here the nuclear shape factor. The form factors are listed in table 3.3 [22]. The shape factor is written as

$$S(E) = 1 + c_0 + c_1 + \frac{c_{-1}}{E} + c_2 E^2 \tag{3.26}$$

where the terms depend on the form factors and nuclear decay variables. The dependence

Table 3.3: Nuclear form factors.

Form Factor	Name	Value
c_{1h}	Gamow-Teller matrix element	0.253 [11]
c_{2h}	Second forbidden matrix element	0.755 fm^2 [22]
b_{WM}	Weak magnetism	43.4 [11]
d	Induced tensor term	40.5 [11]

of the coefficients c_i is given by[22]

$$
\begin{aligned}
c_0 &= -\frac{2E_0}{M_{ave}}(1+\frac{d}{c_{1h}}+\frac{b_{WM}}{c_{1h}})+\frac{2c_{2h}}{9c_{1h}}11m_e^2 \\
c_{-1} &= -\frac{m_e^2}{3M_{ave}}(2+\frac{2b_{WM}}{c_{1h}}+\frac{d}{c_{1h}})-\frac{2c_{2h}}{9c_{1h}}2m_e^2E_0 \\
c_1 &= \frac{2}{3M_{ave}}(5+\frac{b_{WM}}{c_{1h}})+\frac{2c_{2h}}{9c_{1h}}20E_0 \\
c_2 &= -\frac{40c_{2h}}{9c_{1h}}
\end{aligned}
\tag{3.27}
$$

Three of the form factors, b_{WM}, d and c_{1h} are extracted from experimental data. c_{2h} is calculated from nuclear theory. The extraction of c_{1h} depends on the ft value and is [11]

$$
c_{1h}^2 = \frac{2ft_0}{ft_{20}} \tag{3.28}
$$

where ft_0 is the ft value of the Fermi super-allowed β decays, and ft_{20} the average of the ft values of the decays of ^{20}F and ^{20}Ne. This gives a value of 0.254 ± 0.004 [11]. The weak magnetism, b_{WM}, is of special theoretical interest.

3.4.7.1 The Weak Magnetism

The form factor having the largest effect is the weak magnetism form factor. It can be calculated from the $M1$ analog gamma-ray decay strength. This decay strength is from the 10.275 MeV analog state to the 1.634 MeV first excited state in ^{20}Ne. This is a 2^+ to 2^+ angular momentum transition, and a 1 to 0 isospin transition. The decay strength, Γ_{M1}, can be used to extract b_{WM}. This extraction is

$$b_{WM} = \sqrt{\frac{6\Gamma_{M1}M^2}{\alpha E_\gamma^3}} \tag{3.29}$$

where M is the nuclear mass and E_γ the energy of the gamma ray. This gives a value of 43.4± 1.2 [11].

Getting a measurement of this value is of interest for two reasons. One, it tests the Conserved Vector Current (CVC) hypothesis. This hypothesis states that the weak interaction possesses a universal strength and a universal $V - A$ form [27]. In decays involving a $T = 1$ multiplet, the form of the calculation is equation 3.29. This is the largest of the nuclear corrections, and can be determined from experimental data, which has a much smaller uncertainty than any theory calculations. The second reason is more experimental. It gives a parameter with which to benchmark the measuring techniques and the analysis. If the analysis produces the expected value of b_{WM}, the same procedure should give a reliable value for b_{GT}.

3.4.7.2 The Induced Tensor Form Factor

From equation 3.27, the induced tensor form factor d contributes to the corrections much in the same way as the Fierz term. This form factor was measured by combining two data sets [11]. Both the decay of ^{20}F and ^{20}Ne were used to measure d. One data set was the alignment of out-going electrons. The alignment is a higher order polarization. To describe the alignment, the nuclear form factors are needed. The measured alignments of both ^{20}F and ^{20}Ne were added to eliminate the form factors that changed sign between the two nuclei. To eliminate the remaining form factors other than d, an existing gamma-beta angular correlation measurement of both nuclei was added. This gave a value of $d/Ac_{1h} = 8.00 \pm 0.73$.

Using $A = 20$ and $c_{1h} = 0.253$, this gives $d = 40.5 \pm 3.7$.

3.5 Summary

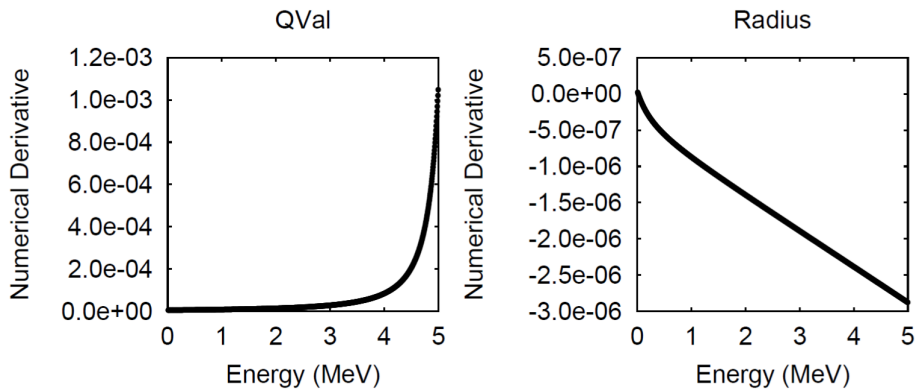

Figure 3.3: The numerical derivative of the ratios in 1/MeV. This is to check how sensitive the shape of the theoretical spectrum is to the uncertainty of the parameters extracted from experiment. These derivatives are an order of magnitude smaller than the 10^{-2}/MeV of the c_1 of the shape factor.

Before the theoretical corrections were fed into a Monte Carlo simulation, the uncertainties from the experimentally determined quantities R and Q was checked. The corrections and phase space were calculated with the central value of both parameters. Then, two more spectra were calculated. One was calculated with $R + eR$ instead of R, and the other was calculated with $Q+eQ$ instead of Q. Here, eR is the uncertainty of R and eQ the uncertainty of Q. Two ratios were taken, which were $[PS(E,Q)C(E,Q,R+eR)]/[PS(E,Q)C(E,Q,R)]$ and $[PS(E,Q+eQ)C(E,R,Q+eQ)]/[PS(E,Q)C(E,Q,R)]$. These results are shown in figure 3.3, where it is seen the change of shape induced is small. The largest value of the numerical derivative is at the end point of the ratio of Q. Even there the ratio is smaller than the terms of the shape factor. These results were further verified by generating a spectrum with a b_{WM} and a b_{GT}. This spectrum was fit with an additional generated spectrum with

R or Q adjusted by one unit of uncertainty. The change in the fit parameter was found to be smaller than the expected statistical uncertainty. With all these corrections, the experiment can be described to the required accuracy.

Chapter 4

Experimental Setup

The experiment was run at the National Superconducting Cyclotron Laboratory (NSCL) in East Lansing, Michigan from September 1, 2015 to September 7, 2015. The experimental technique avoids many of the systematic effects that were important in previous shape measurements in ^{20}F.

4.1 Experimental Technique

The technique used was a calorimetric technique, where the isotope of interest is implanted inside a detector. This reduced several effects that could otherwise distort the beta energy spectrum.

With the calorimetric technique, the radioactive nucleus is surrounded by detector material. As long as the nuclei are implanted deep enough, the electrons will not have enough energy to escape the detector. Even if the electron scatters several times, it still deposits all its energy. This range depends on the detector material. Since any dead layers are at the surface, the decays inside the detector do not see them. A 4π angular coverage is also obtained, as the detector material surrounds the source completely.

There are some caveats for a calorimetric technique. The first is that a large enough detector is needed, since otherwise the electrons could escape at high energies. A large effect is that electrons moving through the detector material will emit a lot of bremsstrahlung.

Using a low-Z detector material will lessen this effect. However, Monte Carlo detector simulations can describe the production and absorption of bremsstrahlung well enough to allow for a precision beta spectrum measurement [28]. Another issue is that accelerators used to generate the isotope of interest must be able to create them at high enough energy in order to implant the isotopes deep enough into the detector. This limits what nuclei can be used for this technique. The act of implanting the nuclei gives the detector a lot of energy. This means that an implant and decay cycle is needed for this experimental technique.

For this experiment, a beam of ^{20}F, was implanted into two different detectors, which were used to cross-check different systematic effects. One was a CsI(Na) scintillator detector, and the other was a EJ-200 polyvinyltoluene (PVT) scintillator detector. After an amount of ^{20}F was implanted, the beam was turned off by dephasing the RF that drove the cyclotrons. Then, the ^{20}F was allowed to decay inside the detector. Given the half-life of ^{20}F of 11 s, the measuring time was varied between 22 and 60 s.

4.2 The ^{20}F Beam

The beam of ^{20}F was created at the coupled cyclotron facility at the NSCL. The primary beam of ^{22}Ne was accelerated by the coupled cyclotrons to 150 MeV/A. A typical intensity of the primary beam was around 60×10^{-5} pnA. It was impinged on a 188 mg/cm^2 Be target and sent through the A1900 fragment separator. The resulting ^{20}F beam was at an energy of 130 MeV/A. The intensity of the ^{20}F was about 2×10^{-5} pnA. The beam was sent to the experimental vault were the detectors were sitting.

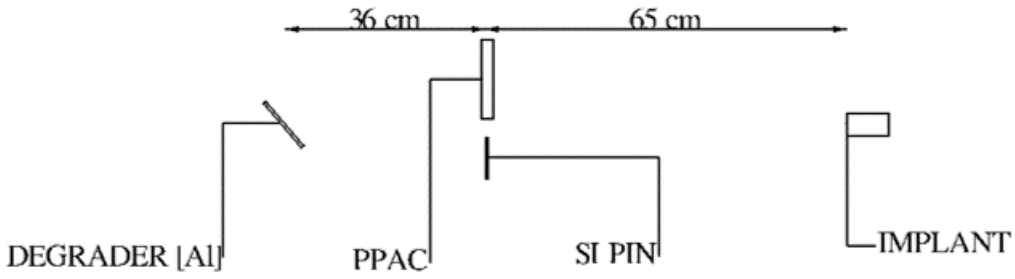

Figure 4.1: A sketch of the location of the detectors upstream of the implant detector. The detectors are not to scale.

4.2.1 Beam Size and Location

To test the size of the beam, a parallel plate avalanche counter (PPAC) was used. The size of the detector was 10 cm by 10 cm square. It was placed 65 cm upstream of the detector. A horizontal and vertical grid was in the detector. Depending on where on each of the grids the particles hit, different charges were sent to either end of the PPAC. The signals were fed into a digital data acquisition system, and read out as an energy. The difference of the two signals divided by the sum was interpreted as a position. The location of the PPAC and other detectors are shown in figure 4.1.

To calibrate the PPAC, a mask with several holes was used. This mask covered the front of the detector, and an alpha decay source in the vacuum was placed in front of the PPAC. Then, everything was left to run until an image of the mask was formed. The mask had holes in it every 1 cm. It also had a large L shaped hole so that the orientation of the mask could be seen. With this, the PPAC could be calibrated.

Before taking data for the beta energy spectrum measurement, the PPAC was inserted into the beam. After adjusting the parameters of the upstream beam optics, the final beam

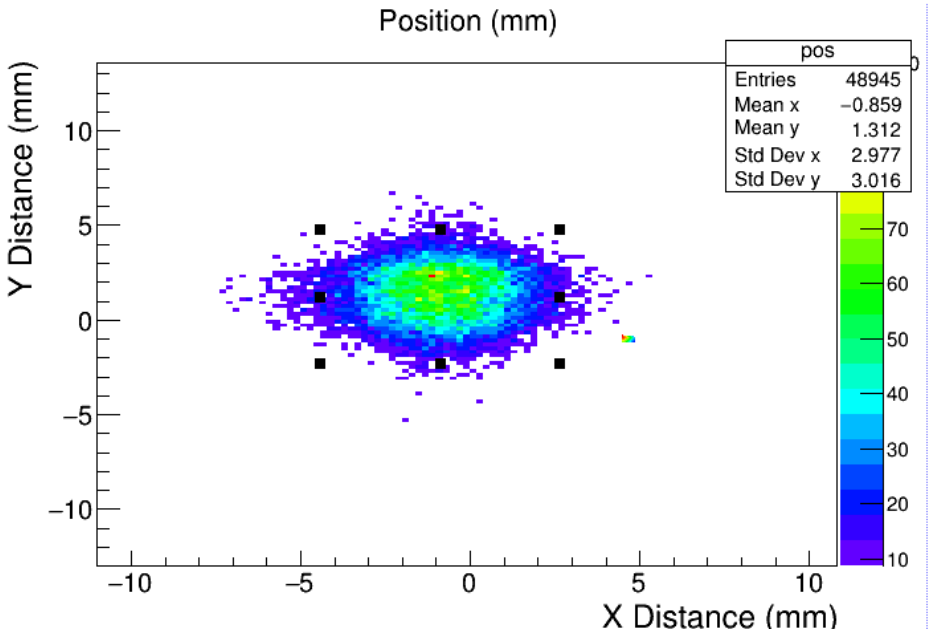

Figure 4.2: The beam spot of the calibrated PPAC spectrum. The samples of the spectrum that were averaged together are shown in the black dots. The center of the fit is not shown.

size at the PPAC was measured. The calibrated data of the signals was built into a 2-D histogram. There was some ringing in the PPAC. To suppress this ringing, a threshold for the PPAC was applied. To calculate the threshold, the peak of the beam spot was fit with a 2-D Gaussian function The centroid of the Gaussian and the sigma in the x and y direction was taken. From the standard deviations, the half widths at half maximum (HWHM) in both directions were calculated. Using the HWHM and the center of the Gaussian, 8 points were selected. These eight points are the black dots in figure 4.2. The z values of the PPAC distribution at each of those points was averaged. This value was the threshold above which the PPAC distribution was plotted. The resulting width was read off to be 8×6 mm.

This is the size of the spot at the location of the PPAC. Ion optics simulations were used to build the envelope of the beam at the PPAC and at the target. Using these cross sections, the magnification between the two locations was calculated. The magnification was different for the x and y directions. With these magnifications, the beam spot at the stopping position

was deduced to be 3.6 × 3.5 mm.

For the depth of the implantation of the beam, ion simulations were used. The LISE++ program was fed the geometry and the settings of the beam magnets. It was given the energy of the beam and the location of the implant detector. It then calculated the depth of the implantation in the detector and the range of the depth inside the detector. This gave a depth of 3.02 cm in side the PVT detector and a depth of 1.156 cm in the CsI(Na) detector. The range straggling was 1.2 mm in the PVT detector and 0.4 mm in the CsI(Na) detector.

4.2.1.1 Verification of Implantation Depth

In order to verify the simulations for the beam implantation depth, a degrader was inserted into the beam for a beam depth measurement, which is shown in figure 4.3. The degrader was made of aluminum and had two different thicknesses: 7.89 mm and 11.38 mm. The beam was caught by a CsI(Na) scintillator of a similar design to the one used during the main measurement. The angle of the degrader was changed to change the effective thickness of aluminum that the beam had to travel through. By comparing the measurement to the one predicted to stop the beam outside of the detector, the depth of implantation could be verified. This was done after the main run, and the simulation matched the measurement. The two are plotted side by side in figure 4.3.

4.3 Detector Configuration

4.3.1 Detectors

One implant detector was a scintillator 3”⌀× 3 ” cylinder of EJ-200 polyvinyltoluene (PVT). It was glued to a clear acrylic disk glued to a photomultiplier tube. The plastic detector

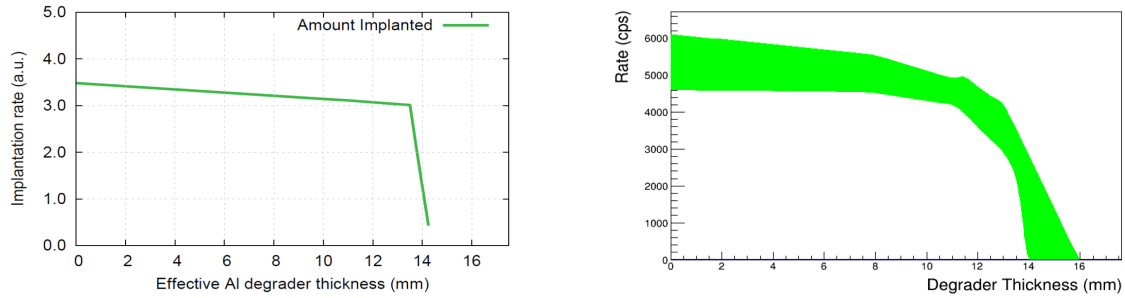

Figure 4.3: The simulation is on the left. The data is on the right. All the fluorine is blocked after 14 mm of degrader.

signal is fast (around 10 ns wide) which makes pile-up a lesser concern. This detector was built by collaborators from Wittenburg University. During the experiment, the voltage on the PMT of this scintillator was varied and a gain monitoring system was installed.

To monitor the gain of the plastic detector, an acrylic disk containing an optical fiber was placed between the crystal and the photomultiplier tube. The other end of the fiber was fed into a box with a LED driven by a function generator, which ran at a trigger rate of 500 counts per second. The function generator produced two pulses separated by 136 μs. These two pulses had different amplitudes, so that the gain drift could be monitored by observing the drift from two different energies. The box was made light-tight with electrical tape and black paint. An additional optical fiber fed the light to a Si PIN diode. This was to monitor the light output of the LED. A sketch of the PVT scintillator including the acrylic disk is shown in figure 4.4.

To check for systematics effects, another implant detector was used. It was a 2" $\times$ 2" $\times$ 4" CsI(Na) detector. This detector was a module from the CAESAR array [29]. It does not have any gain monitoring like the PVT detector.

In order to measure the gamma ray from the ^{20}F decay, a frame was built to hold four 3" $\times$ 3" $\times$ 3" CsI(Na) detectors. These were also part of the CAESAR array. The frame to

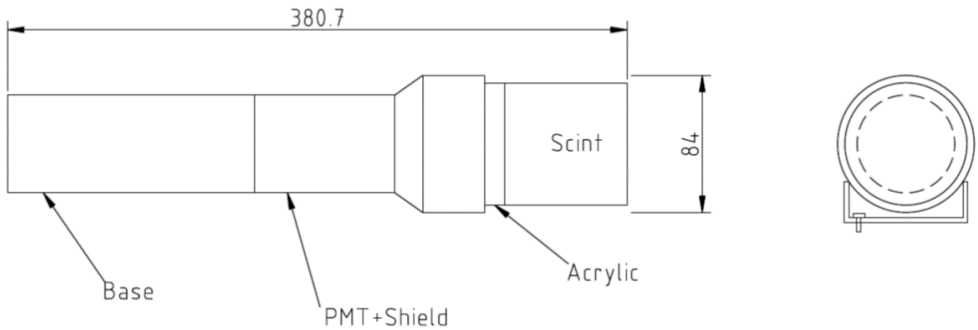

Figure 4.4: A sketch of the PVT implant detector. The acrylic disk is seen along as PVT scintillator. The scale is in mm.

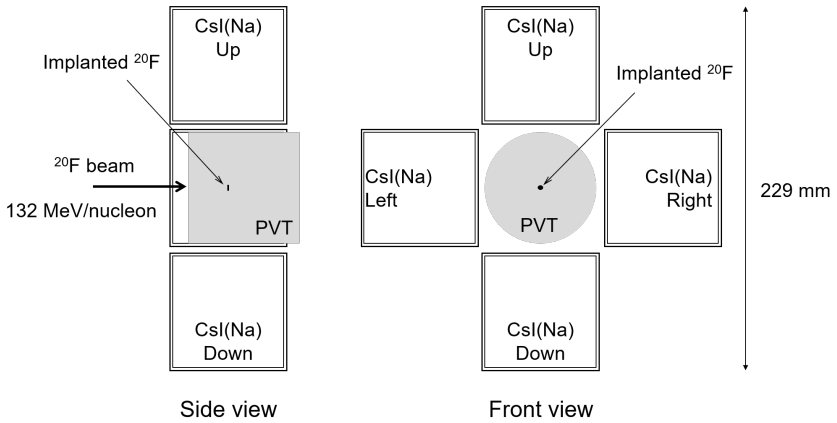

Figure 4.5: A sketch of the PVT implant detector set up. Notice that the PVT detector fills up the space between the gamma detectors.

hold the four detectors was designed to be able to move the four outer detectors around. A sketch of the PVT implant detector configuration is shown in figure 4.5. A sketch of the CsI Implant detector configuration is shown in figure 4.6.

To switch between different implant detectors, the central detector in the frame was removed and put on the floor. The other detector was placed in the center of the four gamma detectors. The PVT detector was supported on a metal rail, while the CsI (Na) detector was supported on pile of scrap aluminum. Pictures of both detector set ups can be see in figure 4.7.

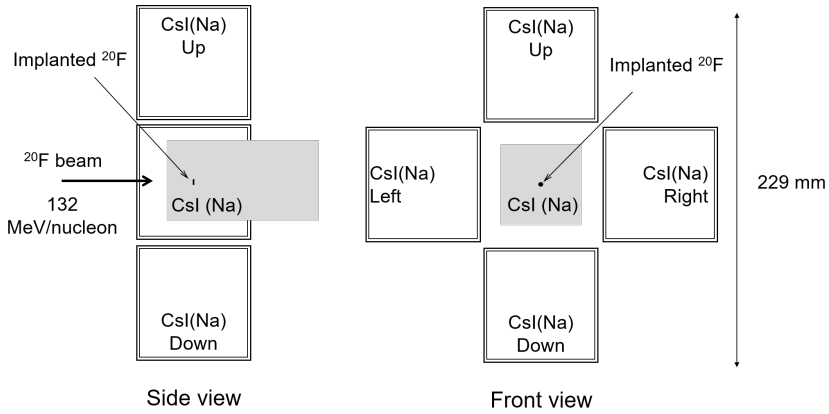

Figure 4.6: A sketch of the CsI(Na) implant detector set up. The CsI(Na) detector is recessed 1 inch.

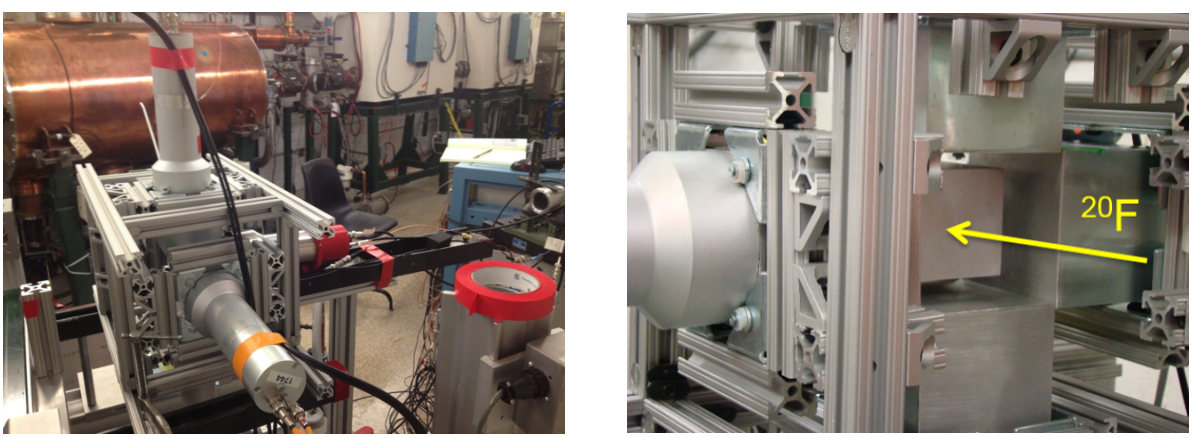

Figure 4.7: On the left the PVT set up can be seen. The rail the detector sits on and the optical fibers (the black cords) can be seen. On the right the CsI(Na) set up can be seen. In the center the implantation detector is seen.

4.3.2 Powering the Detectors

To power the gamma and implant scintillators, three 2-channel NHQ 212M ISEG power supplies were used. The Si detector was powered by a Tennelec TC248 amplifier. The PPAC was powered by an integrated power supply.

Each detector had a different voltage. The PVT implant detector was varied in voltage over the course of the experiment. Initially, the high voltage on the PVT detector was chosen to take advantage of the dynamic range of the detector. Due to concerns about the beta energy spectrum shape, the voltage on the PVT detector was changed to several values as the experiment went on. For the PPAC, the voltage setting was adjusted to get a large enough signal. The voltage for the four gamma detectors was chosen so that they had roughly the same gain. The voltages of the detectors is shown in table 4.1.

Table 4.1: Detector voltages.

Detector	Power Supply Setting (V)
PVT Implant Setting 1	-975
PVT Implant Setting 2	-856
PVT Implant Setting 3	-780
CsI (Na) Implant	780
CsI (Na) Gamma 1	930
CsI (Na) Gamma 2	1000
CsI (Na) Gamma 3	970
CsI (Na) Gamma 4	1015
Si Pin	20
Pin diode	15
PPAC	560

During the implantation cycle, a large amount of current was generated in the implant detectors. In order to counteract this, a limiter box was installed. The limiter box had several relays that reduced power to the PVT detector's photomultiplier tube during the beam-on cycle. To accomplish this, the limiter box was given the same signal that fed the

beam-on/beam-off for the cyclotrons. For the CsI(Na) implant detector, the high voltage supply had the current limiter enabled. The power setting was not changed for the CsI(Na) implant detector.

4.4 Experimental Conditions

The data was taken in runs of roughly one hour. However, many runs were cut short when the DAQ stopped recording data for one of the detectors. This was usually the up gamma detector, and was correlated with the start of a new implant cycle. In order to properly measure the decay, the beam was pulsed with an implantation time of anywhere from 1 to 2 seconds, and a decay time ranging from 22 s to 32 s. The beam was turned off since the light from the implantation of the beam would drown out any signal obtained. A run with a decay time of 60 seconds was also taken for each implant detector.

To achieve the beam pulsing, two timer boxes were used. A CAEN N1145 quad scaler module was used to control the beam-off time. This module had a digital control of time down to 1 ms. Once the the time finished counting down, a signal was sent to a second module. A CAEN N93B dual timer used the signal from the quad scaler as a start signal. The beam-on time period was set with an oscilloscope, which was less precise. Once the dual timer finished its time, it sent a signal back to the quad scaler to restart the cycle. The output of these two modules created a signal with one voltage level during the dual timer's time and another voltage condition during the quad scaler's time. This signal was sent to the cyclotron control room. There, the voltage level during the quad scaler's time dephased the cyclotron RF, turning the beam off. When the dual timer voltage level occurred, the RF returned to the tuned value, turning the beam on. A flowchart showing the timing circuit is

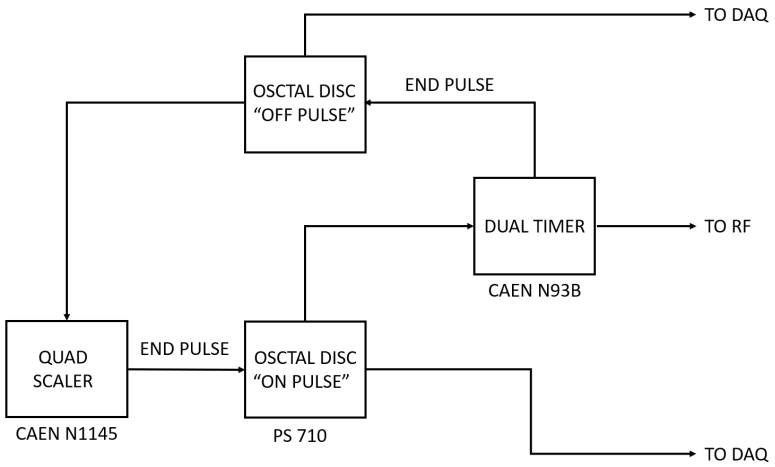

Figure 4.8: The modules used for the timing. "Disc" stands for discriminators.

shown in figure 4.8

Chapter 5

Data Processing

A digital data acquisition (DAQ) system was used to record the data for this experiment. To configure the DAQ, the detector signals were looked at using an oscilloscope in order to get the decay time. The input parameters of the energy filter were tuned from the decay time of the signals.

5.1 Data Acquisition

All the signals for all the detectors were sent to 16 channel XIA (X-ray Instrumentation Associates) Pixie modules. Each channel had a 250 mega-sample per second digitizer. The incoming signal was first digitized, and then processed by the module. The modules were run with the NSCL firmware. A list of the three modules and which channel processed the signals from which detector is seen in table 5.1. For module 2 channel 0, the digitized wave-form was recorded over 400 ns. The clock used for the digitizers was a stable EPSON SGR-8002JC programmable crystal oscillator. The first thing the Pixie modules did was to digitize the wave forms of the signals. The digital wave forms of the signals were only saved for the PVT implant detector. The Pixie modules' software applied a trapezoidal energy filter to the digital wave-forms. Each of the channels gave a time stamp and an energy calculated from a trapezoidal filter.

Table 5.1: DAQ cabling Scheme.

Module	Channel	Detector
0	0	PVT Implant
0	1	CsI(Na) Implant
0	4	Large CsI(Na) Up
0	5	Large CsI(Na) Left
0	6	Large CsI(Na) Down
0	7	Large CsI(Na) Right
0	8	Beam-on Signal
0	9	Beam-off Signal
0	10	100 Hz Pulser
0	11	PVT Gain Monitoring Pulser
1	0	PPAC Up
1	1	PPAC Down
1	2	PPAC Left
1	3	PPAC Right
1	8	Beam-on Signal
1	9	Beam-off Signal
1	10	100 Hz Pulser
1	11	PVT Gain Monitoring Pulser
2	0	PVT Implant (With Digitized Wave Forms)

5.1.1 Trapezoidal Filter Description

In order to get timing and energy information for the digitized signals, a trapezoidal filter was applied. After the parameters of the filter were set, the filter was taken on the digitized detector signals. First, three sums of the digitized wave-forms were taken. The first sum was over a time known as $t_{PEAKING}$. Then, a second sum was taken directly after the first over a time known as t_{GAP}. Then, a third sum was taken directly after the the second with over a period of $t_{PEAKING}$ again. These three sums were associated with weights given as [30]

$$E = C_0 \times S_0 + C_g \times S_g + C_1 \times S_1 \tag{5.1}$$

with E being the energy of the signal, S_0 being the first sum over $t_{PEAKING}$ described above, S_g being the sum over t_{GAP}, and S_1 being the second sum over $t_{PEAKING}$. C_0 is given by

$$C_0 = \frac{-(1 - e^{\frac{t_{SPL}}{\tau}})e^{\frac{t_{PEAKING}}{\tau}}}{1 - e^{\frac{t_{PEAKING}}{\tau}}} \tag{5.2}$$

where $t_{PEAKING}$ is the time described above, t_{SPL} is the 8 ns sampling time, and τ an additional parameter. C_g is

$$C_g = 1 - e^{\frac{t_{SPL}}{\tau}} \tag{5.3}$$

Finally, C_1 is

$$C_1 = \frac{1 - e^{\frac{t_{SPL}}{\tau}}}{1 - e^{\frac{t_{PEAKING}}{\tau}}} \tag{5.4}$$

This filter averaged the background before a pulse in C_0 over $t_{PEAKING}$. It took a sample of the pulse, averaged over $t_{PEAKING}$ again in C_1. Then, it subtracted off C_0 from C_1, after adjusting for the exponential decay of the pulse. The time constant of that decay is the τ parameter. When tuning the filter, the τ parameter had the largest effect. For logic signals which do not decay, the τ parameter was very large. For this experiment, the various filter parameters are summarized in table 5.2. There was also a trigger filter in the Pixie system. The expression in equation 5.1 is the same, but the parameters are shorter. There was a threshold that the output of the trigger filter had to be above in order to be recorded. These values are shown in table 5.3. The trigger filter was used to calculate the time stamps of the events.

Table 5.2: Energy filter parameters.

Detector	τ	$t_{PEAKING}$	t_{GAP}
PVT implant	60 ns	208 ns	128 ns
All CsI (Na) detectors	900 ns	480 ns	48 ns
PPAC channels	300000 ns	1200 ns	96 ns
Si PIN	50000 ns	1744 ns	96 ns
Beam-on/beam-off signals	1000000 ns	400 ns	96 ns
Pulser	5000000 ns	400 ns	96 ns
Light pulser	150 ns	608 ns	96 ns

Table 5.3: Trigger filter parameters.

Detector	$t_{PEAKING}$	t_{GAP}	Threshold
PVT implant	104 ns	104 ns	30
All CsI (Na) Detectors	200 ns	72 ns	20
PPAC Channels	904 ns	104 ns	200
Si PIN	400 ns	80 ns	100
Beam on/beam-off signals	104 ns	40 ns	20
Pulser	104 ns	40 ns	20
Light pulser	104 ns	72 ns	35

5.1.2 Data Acquisition Software

In order to set the parameters of the various filters, a program called NSCOPE was used [31]. The program was used to set the rise time, the gap, and the threshold for both the energy filter and the trigger filter. These parameters were set differently for each detector type. The CsI(Na) detectors (the implant and the 4 gamma detectors) shared the rise time and gap time, while other detectors had different parameters. Sample spectra were taken with NSCOPE, and the parameters saved to a file.

This file was loaded with a program called ReadOut, which ran the data taking. The ReadOut program used a ringbuffer in order to record the output of the data. The program recorded data as an .evt binary file if the record option was selected.

The ringbuffer was also fed to a program called scalers. This gave the rates of the events coming into each channel. It gave an input rate to each channel, the recorded rate, and the

total over each run. This was to check if every channel in each module was still recording data.

For online analysis, a program called SpecTcl was used. It took the .evt files and processed them into histograms. These histograms could be put in coincidence. The implant detector energy and rate were displayed. The energy of the implant vs time was also displayed. Additionally, the implant energy vs time since last beam-on was plotted as a 2-D spectra. The decay curves were also plotted. These were built by histogramming the time stamp in the detector relative the time since the last beam-on. These histograms were used as diagnostics. The program allowed for building spectra with coincidence conditions.

5.2 Data Taking and Processing

To take data, the ReadOutGUI program was activated. Data was taken in one hour intervals called runs. If a channel stopped counting, the run was ended before one hour was up. The events built by Readout had a time interval of 8000 ns.

Each run generated one or more .evt files. The resulting .evt files of ReadOut were processed using a program called DDAS dumper. This converted the .evt files to ROOT files. One .evt was dumped to one .root file. These ROOT files contained a TTree that had the energy and time stamps of each detector. The information was saved event by event and sorted by time. It was formatted in a C++ class called DDASEvent. This event class contained data for each channel from the data acquisition. The energy was given out in ADC units and was not calibrated. These units had a range from 0 to 32767. The time was given in counts of DAQ clock. The digitized wave forms were also saved in this event.

From the ROOT files produced by the ddasdumper, another ROOT file was built. All

the ROOT files from one run were built into one new ROOT file. These files were processed with a modified version of a program called scan. The original version was written by Stan Paulauskas. The TTree was looped over event by event. For each event, each channel was looped over. For the first event and first channel, the time integer was recorded. This first time was subtracted from all subsequent time stamps. The time differences were multiplied by 8 ns to turn them into time in seconds. Then, the various energies and times for each detector were built into histograms for each channel. During looping through the events, the energy and times for the implant detectors, four gamma detectors, beam-on signal, and beam-off signals were saved to a variable. This information was used to build new events for a new TTree.

Each event started with a non-zero energy reading in any of the five detectors. Then, a 400 ns long time gate opened, during which all energies and times were saved into the event. The time signatures of the last beam-on and beam-off signals were also saved into each event. The beam-on and beam-off signals were logic Nuclear Instrumentation Module (NIM) signals.

Chapter 6

Half-life Measurement

6.1 Motivation

During the experiment, it was noticed that there was a disagreement between the value of the half-life measured and the value in the literature. As a side project and as a first chance to thoroughly investigate the data, a half-life analysis was made. These results have been published [32]. The previous measurements of the half-life of ^{20}F are shown in figure 6.1.

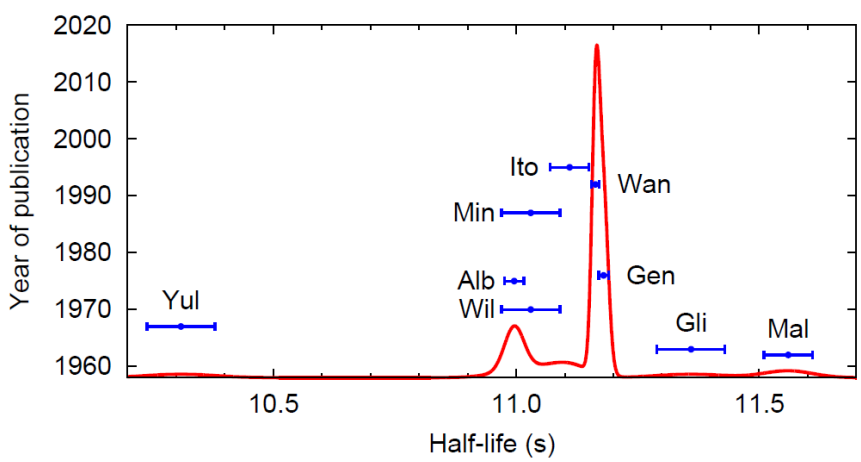

Figure 6.1: Previous measurements of the ^{20}F half-life. The labels correspond to: Mal [33], Gli [34], Yul [35], Wil [8], Alb [9], Gen [36], Min [37], Wan [38] and Ito [39].

This ideogram has a red line which is a sum of Gaussian functions. The centroids of the Gaussians are the central values of the measurements. The sigmas are the errors, and each Gaussian is weighted by $1/\sigma^2$. It is seen that there are two different values that the half-lives are converging to.

6.2 Half life Data Analysis

First, the data was processed as described in the previous chapter.

6.2.1 Data Selection

Only the data from the PVT implantation set was used for the half-life analysis. The PVT data was separated into 7 sets. A summary of the set conditions is shown in table 6.1. As shown in the table, the major conditions were the PVT high voltage, the inhibitor box, and the beam current.

Table 6.1: Settings for the PVT runs.

Set	Beam-on Time [s]	Measuring Time [s]	PVT HV [v]	HV Inhibit Installed	Beam intensity [nA]	Runs
1	1.67	30	-975	No	30	9
2	1.67	30	-975	No	93	2
3	1.67	30	-975	Yes	30	9
4	1.67	30	-975	Yes	93	11
5	1.67	30	-856	Yes	30	93
6	1.00	60	-800	Yes	93	1
7	1.10	20	-780	Yes	93	10

The inhibitor box was not installed until the third set of data. The inhibitor box reduced the high-voltage by about 100 V during the beam-on period. Without the box, the current on the PMT was saturated during the beam-on period. This caused a gain shift over time as the power supply recovered. This time-dependent gain shift caused large systematic errors when the beta cuts were moved. The beta cuts are the energy conditions imposed on the implant detector when the coincidence was imposed. Thus, sets 1 and 2 were not used in the final analysis, but are listed here for completeness's sake. These gain shifts can be seen in figure 6.2.

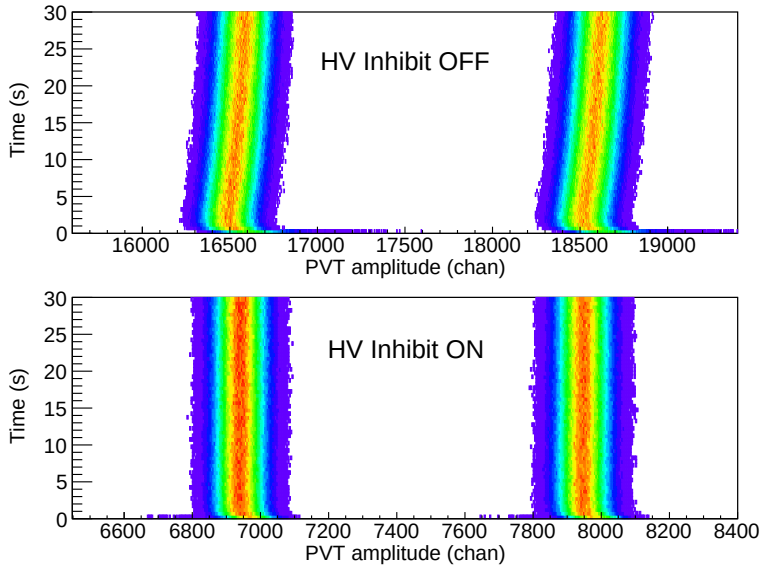

Figure 6.2: The light pulse as a function of time for set 1. The gain changes smoothly over time. This causes a large change in the half-life as the beta cuts are moved.

6.2.2 Cut Selection

In order to do the half-life analysis, software coincidences were imposed. Three conditions were set in total. Two conditions were on the energy in the implantation detector and one of the four CsI(Na) detectors. The gamma cuts are summarized in table 6.2. These are the energy cuts imposed on the four gamma detectors when the coincidence was imposed. An additional condition was imposed on the time difference between the events recorded in the two detectors. A sample spectrum of the gamma and beta energies is shown in figure 6.3.

Table 6.2: Energy cuts for the gamma detectors.

Detector	Lower Cut [ADC units]	Upper Cut [ADC units]
Up	1350	1650
Left	1280	1600
Down	1440	1800
Right	1450	1800

Fixed energy gates were used to select in the beta window for the PVT run sets. Each different data set had a different energy window adapted to the gain. A sample spectrum

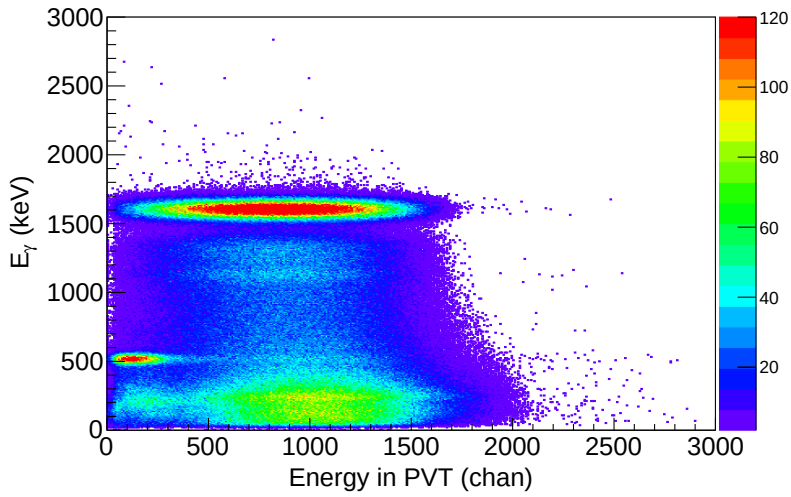

Figure 6.3: The y axis shows the gamma detector energy. The x axis is the implant detector energy. The ^{20}F coincidence region can be seen towards the top of the spectrum. The region at 511 keV can be seen closer to the bottom of the figure.

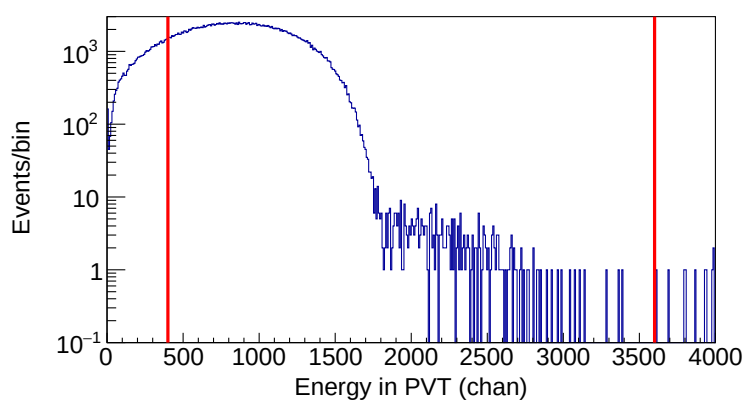

Figure 6.4: A beta spectrum built by applying the gamma cuts and time difference cuts. The beta cuts for the half-life analysis are shown as the red lines. The lower beta cut was selected to be above the 511 region. The upper beta cut was selected to include all the pile-up.

with the gates can be seen in figure 6.4. These cuts varied from set to set. A summary of the PVT energy cuts can be seen in table 6.3. This spectrum was put in coincidence with the gamma spectra. The lower beta cut was selected to cut out the 511 keV distribution as seen in figure 6.3. When gated around that energies, the resulting gammas measured by the other large CsI(Na) detectors are consistent with ^{10}C and ^{11}C. This comes from the break-up of

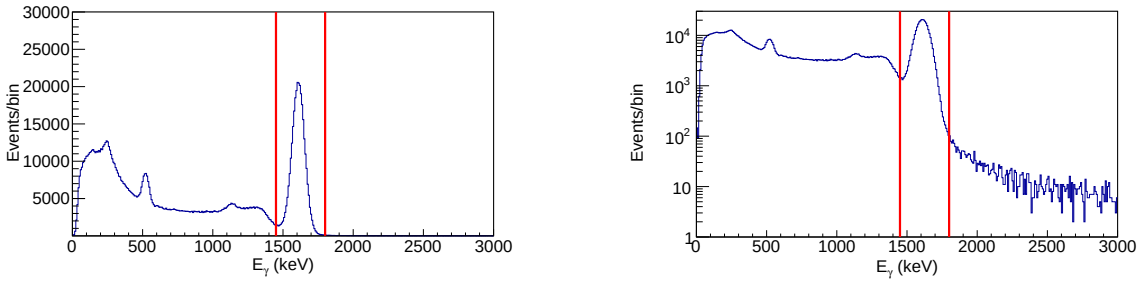

Figure 6.5: The red lines show the gamma cuts, which were chosen to reduce the effect of the rate dependent gain. On the left the spectrum is seen in a linear scale. On the right the spectrum is seen on a log scale.

the ^{12}C in the plastic scintillator. The lower beta cut was chosen to exclude any potential pile-up from this region.

Table 6.3: Energy cuts for the PVT detector.

Set	Lower Cut [ADC units]	Upper Cut [ADC units]
1-2	2000	14400
3	1500	12000
4	1700	13800
5	800	6200
6	480	4200
7	400	3600

As described above, only the runs after the installation of the limiter box were used for the half-life analysis. This would be sets 3-7.

A condition was set by building a spectrum of the time differences between the implant detector's event and one of the four gamma detector's events. The peak of this time difference spectrum was found, and an interval of ±24 ns was used for this gate. A sample time difference spectrum can be seen in figure 6.6.

The time difference spectrum shows several features. First is the prompt peak, which are a correlated gamma and beta in an event. To the right of the prompt peak, there is a pedestal of events. These come from pile-up events. What happens is that a ^{20}F event

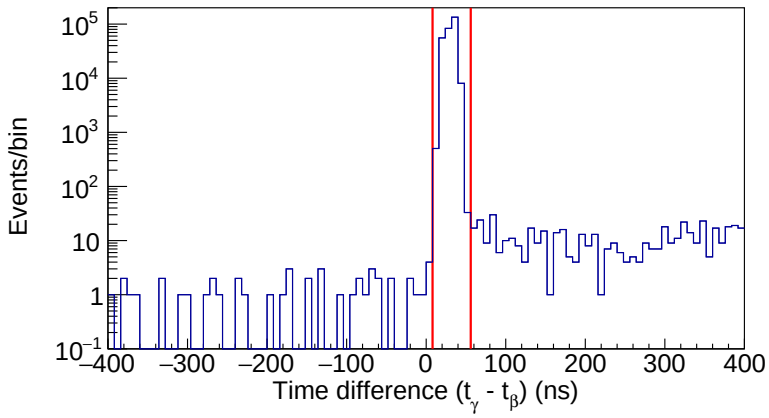

Figure 6.6: The time difference between the up detector and the PVT implant detector. The tail on the right side of the large peak is due to pile-up. The time cuts are shown with a line.

decays and the time stamp of the emitted beta is recorded. The corresponding gamma ray is not detected. Then, within the pile-up window, a second ^{20}F decays. The implant detector is dead and does not record the second beta time stamp. The gamma ray is then detected at a later time compared to the first event. An cartoon sketch of this effect is shown in figure 6.7. The pedestal can be seen in full in figure 6.8.

The other events to the left of the prompt peak and to the right of the pile-up pedestal are accidental coincidences. These include the background coincidences.

The time signals for the outer four gamma detectors were used for the half-life analysis. This gave 4 independent measurements of the half-life per run. Only full decay cycles were used. This was done by finding the last beam-on signal and putting a condition on the run time of the events.

The dead time was corrected using measured rates and a dead time of 464 ns for the implant detector and 656 ns for the gamma detectors. The dead time was measured by building a spectrum of the time difference between consecutive time stamps. The lowest time difference was taken as the dead time. This was checked using the light pulser in the

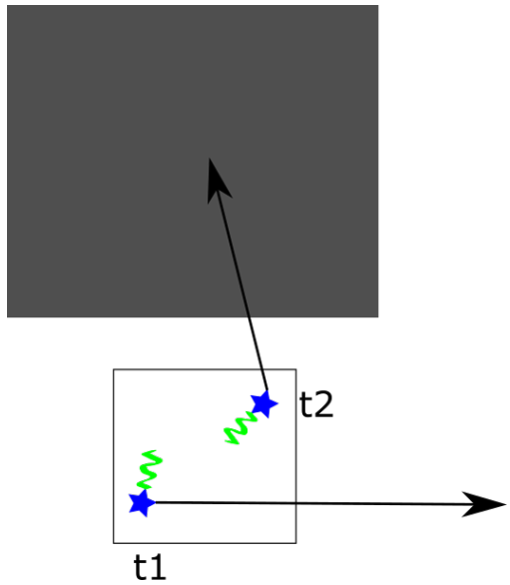

Figure 6.7: A sketch of the pile-up events. A ^{20}F decay happens at time *t1*. The green electron is detected in the implant detector. The black arrow (the gamma ray) is not. Then, later at time *t2*, another ^{20}F decays. *t2* is within the pile-up window of *t1*. Both electrons energies pile-up and are added together. However, the time stamp recorded by the DAQ is still *t1*. The gamma ray from event *t2* can be detected in a gamma detector at time *t2*. This creates the uncorrelated event pedestal in the time difference graph.

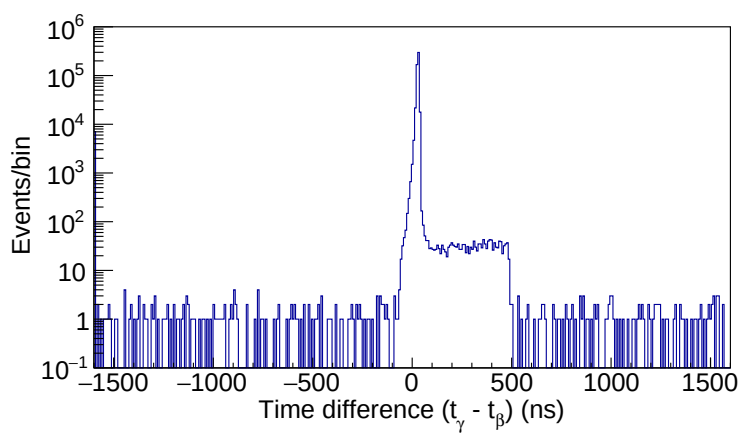

Figure 6.8: The time difference spectrum zoomed out. This figure is built from with energy coincidences with energy cuts.

PVT detector. For each gamma detector, a histogram of the energy-filtered rate was built. The unfiltered implantation detector rate and gamma rate was built. Using the uncorrected rates as an input, the gamma detector rate was corrected for bin by bin. The correction used is

$$r^{c}_{coincidence} = \frac{1}{1 - r_{\beta}\tau_{\beta}} \frac{1}{1 - r_{\gamma}\tau_{\gamma}} r^{m}_{coincidence} \tag{6.1}$$

where $r^{c}_{coincidence}$ is the corrected gamma-beta coincidence rate, r_{β} the raw measured implant rate, τ_{β} the dead time of the implant detector, r_{γ} and τ_{γ} the raw measured rate and dead time for the CsI(Na) detector, and $r^{m}_{coincidence}$ the measured coincidence rate. Then, after corrected for the dead time, each cycle was added together relative to the last beam-off. These stacked cycles were used to find the half-life.

For high beam intensity runs (i.e. sets 4,5 and 7), the dead time corrections had a size of 31 to 36 ms. For low beam intensity runs (i.e. set 3), the dead time correction changed the half-life by 6 to 8 ms. The values shown in this chapter are those with the dead time correction.

Once the decay spectra were put in coincidence and stacked up, it was fit with the function

$$f(t) = a \exp\left(-t \times ln2/T_{1/2}\right) \tag{6.2}$$

where a and $T_{1/2}$ are free parameters. a is the initial rate and $T_{1/2}$ the half-life. The decay curves were fit from 1.5 seconds past the beam-on time to 1.5 second from the end of the decay time. The fitting method used was the log likelihood method. This method was chosen to keep the result independent of the binning of the decay curves. The 60 second decay run up detector result is shown in figure 6.9. From this run, it is seen that the spectra does not decay back down to the background.

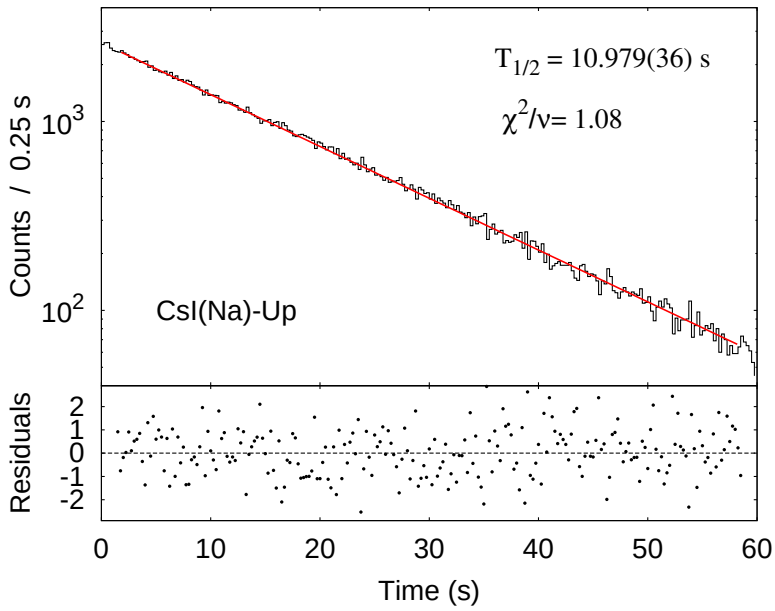

Figure 6.9: The decay spectrum from the up gamma detector is shown on the top graph. The red line is the exponential fit. The bottom graph shows the residuals from the fit.

The decay spectra were built run by run, and the resulting fitting results were averaged together. Runs with a p-value less than 0.05 were considered statistically insignificant and thrown out. After all the significant half-lives were collected, the average of them all was taken.

6.3 Systematic Effects

Several systematic effects were investigated. The dead time correction was applied before any other systematics were investigated.

6.3.1 Dead Time

The timing resolution of the clock is 8 ns. Due to this, there is an uncertainty on the dead times of at least 8 ns. The dead times were varied ±4 ns and the half lives calculated. Half

the difference of those half lives was taken as the systematic uncertainty.

6.3.2 Pile-up Effects

The dead time is over-corrected. Due to pile-up, some of the dead time events are not totally lost. Some of the events thought to be missing just got shuffled around. This is a problem due to the fact that energy gates are imposed. The pile-up events also have a different time structure than the regular events. Due to the fact that the pile-up goes as the singles rate squared, the half-life of the pile-up events is half that of the non-piled-up events. This creates a background with a different time signature, and causes a change in half-life.

The 48 ns time cut around the peak, shown in figure 6.6, was compared to several other, larger time cuts. The narrow time cut still has some uncorrelated background and pile-up events in them.

To account for this effect, several other time cuts were taken. These cuts were plotted vs half-life in figure 6.10. The values were fit with a quadratic function. This function was extrapolated to zero, which was the correction due to the pile-up. The half-life was corrected to the zero value of the window. The difference between this extrapolated value and the previously measured value was taken as a correction and as an error bar.

6.3.3 Background

The first systematic effect is the effect of background. Due to the short measuring window, directly fitting a background is impossible. There is no background region for the fitting function to anchor to, which induces a large correlation between the background and the half-life. Several techniques were used to estimate the background.

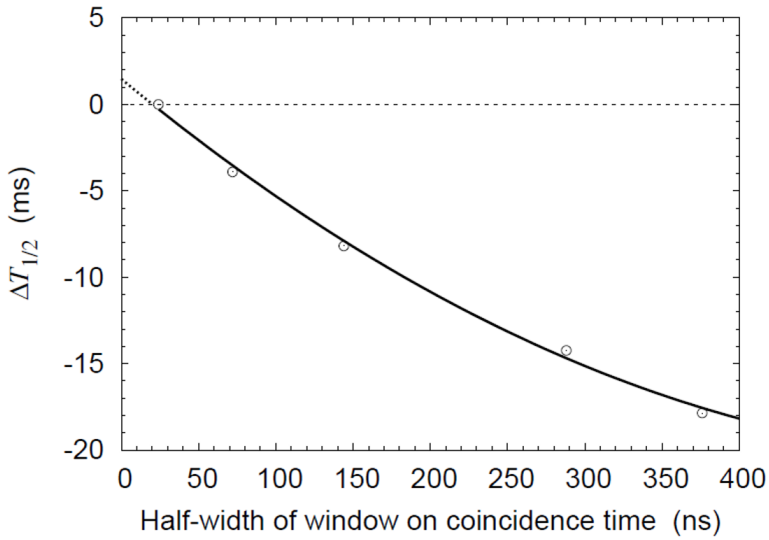

Figure 6.10: Time difference vs the resulting half-life. The line is a quadratic fit which was extrapolated to zero.

6.3.3.1 Simultaneous vs Separate Fitting

The first attempt was by simultaneously fitting each run with a different fitting function. The equation used was

$$f(t) = a(\exp(-t \times ln2/T_{1/2}) + b) \tag{6.3}$$

with b the relative background level. The half-life of the four detectors was set to be a common parameter. The relative background level and initial rate, however, were assumed to be independent for each spectrum. The resulting half-life was compared to the value found with fitting each detector separately without a background.

The effect of adding a background was investigated using Monte Carlo. Exponential functions were generated and an amount of background added. The resulting function was fit with a decay curve without a background parameter. The amount of background added was varied, and the resulting half lives plotted. It was found that increasing the background decreased the value of the half-life, and that the background level and the half-life value were

strongly correlated.

A similar Monte Carlo was written to check the simultaneous fit method. Four decay curves were simultaneously fit the same way was the data. They were also fit separately with only an exponential decay. The background was varied and the difference between the two values was taken. The method shows a trend similar to the one seen in the previous Monte Carlo.

In the data, it was discovered that the results of the simultaneous vs separate fitting depended on the size of the dead time correction. If the dead time was over-corrected, it induced an effect that was similar to having a larger background. If more dead time was imposed, the effect was as if there was a negative background. A dead time correction was added to the Monte Carlo, and a similar trend was seen. As long as the dead time is known exactly, the background can be extracted with this technique.

6.3.3.2 Spectra Arguments

The other way to try and gauge the background size is to look at the spectra. Looking at figure 6.6, it can be seen that on the left side of the large peak, there are very few counts. It can also be seen that the prompt peak in the center contains most of the counts, while there is a long pile-up tail on the right side of the peak.

In the gamma-beta energy 2D plot (figure 6.3), it can be seen that there is no background events aside from the 511 keV region. There are no gamma rays in the 1620 keV window which was filtered on. The only coincidence possible is if there is pile-up into that window along with a beta event. The estimate of those events is shown on the left side of the peak in the time difference figure shown in figure 6.6. These events are accounted for when extrapolating the different time difference cuts, as shown in figure 6.10.

6.3.4 Cut Sensitivity

For each pair of detectors, there were four conditions: two for each the implant and gamma detectors. For the gamma cuts, the edges of the gates were varied $\pm$ 5 keV in each direction for each cut. The results is insensitive to the upper beta cut. The lower beta cut was scanned with 6 different values going evenly from the initial lower beta cut to the peak of the spectrum. Moving the lower beta cut also affects the dead time correction. In order to disentangle the two, the lower beta cut was varied with two different time difference conditions. The location where the difference between the two calculations blows up is where the effect of the lower beta cut starts being swamped by the effect of the pile-up. This is limit of where the lower beta cut was scanned. All four of these conditions were varied independently, and the procedure of generation the spectrum and fitting the decay curves was done. Half the resulting range of half-life values was taken to be a systematic uncertainty.

The fitting range of the decay spectra was varied. The start of the fit was varied bin by bin up to 6.5 seconds into the decay spectrum. The end of the fit was varied the other way to cut out the end of the decay spectrum. Since there was no noticeable systematic effect, there was no increase in error associated with this effect.

6.3.5 Oscillator Stability

The oscillator of the PIXIE board has a stability of $\pm 5 \times 10^{-5}$. All times in the analysis were stretched by this value, and the half-life calculated. Half the difference between the stretched value and the original value was taken as the systematic error.

6.3.6 Binning and Fitting

In order to check the sensitivity of the result to binning, the decay curves were rebinned by a factor of two. Half the difference between the rebinned half-life and the original half-life is considered the correction and the uncertainty.

For the fitting method, log-likelihood estimators were used to fit the summed data. This was done with two different packages which gave identical results. This was compared to analytic results, which gave the same results, so the half-life is insensitive to the fitting method.

6.4 Result and Discussion

The half-lives obtained for all runs and all four detectors are shown in figure 6.11. The results are shown in in table 6.4. The size of the systematic uncertainties investigated are shown in table 6.5. After the dead time correction, the value of the half-life was found to

Table 6.4: Half-life results.

Detector	Half-Life	Error
Up	11.0195	0.0088
Left	10.9944	0.0087
Down	10.9980	0.0085
Right	10.9987	0.0095
Mean	10.9999	0.0044

be $11.0011 \pm 0.0069_{\text{stat}} \pm 0.0030_{\text{syst}}$ s.

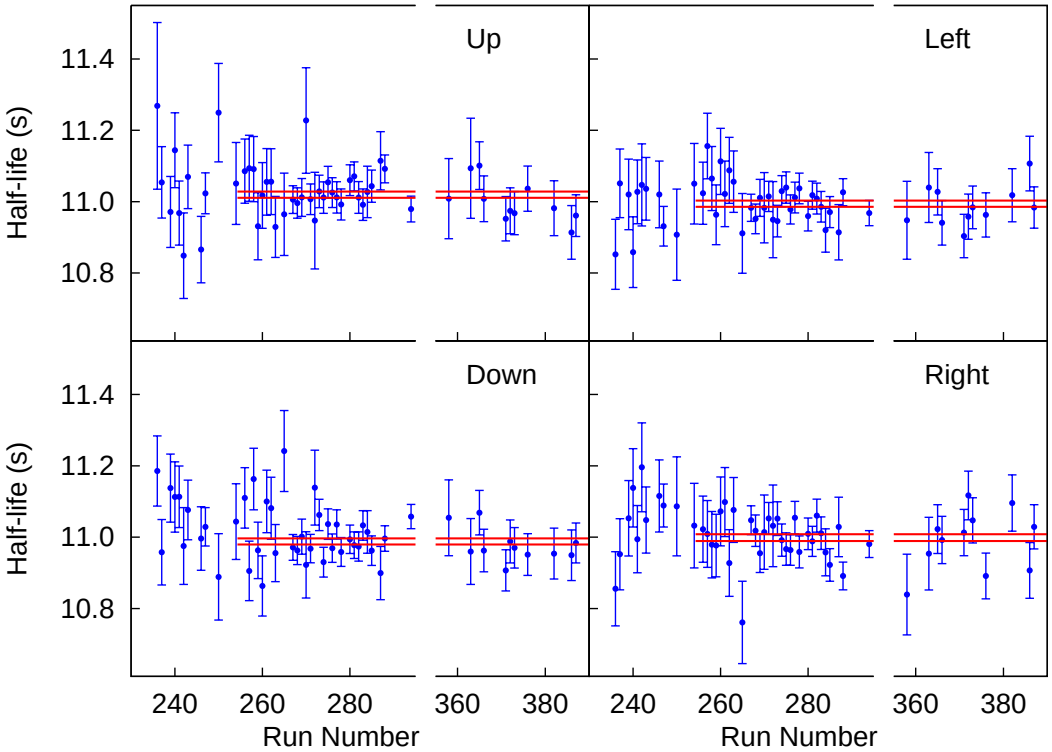

Figure 6.11: The red lines show the results of the fits over the runs that were used. The additional half-lives shown are excluded to reasons discussed previously.

Table 6.5: Systematics.

Source	Correction [ms]	Uncertainty [ms]
Dead-time	0.00	0.24
Oscillator stability	0.00	0.80
Lower PVT cut	0.00	2.32
Lower gamma cut	0.00	0.15
Upper gamma cut	0.00	0.05
Uncorrelated events	1.47	1.47
Binning	-0.30	0.30
Total systematic	1.17	2.89

6.5 Conclusion

The half-life measured is most consistent with some previous measurements of about 11 s.

This can be seen in figure 6.12. This measurement disagrees with the most recent and most

precise measurements.

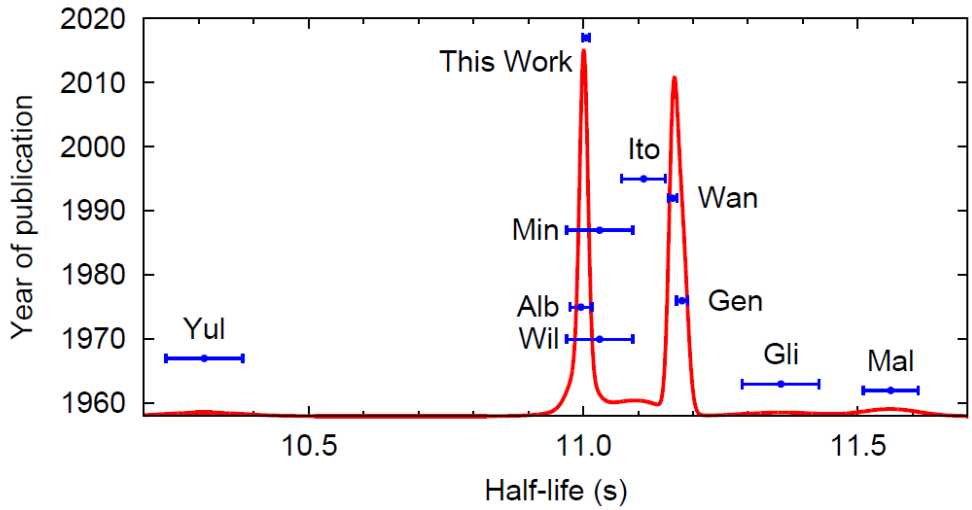

Figure 6.12: A scatter plot of previous values with this work added. The labels correspond to: Mal [33], Gli [34], Yul [35], Wil [8], Alb [9], Gen [36], Min [37], Wan [38] and Ito [39].

Motivated by this measurement, another measure of the ^{20}F half-life has been done by a group at Notre Dame. The outcome of the measurements was 11.0160 $\pm$ 0.0041$_{\text{stat}}$ $\pm$ 0.0155$_{\text{sys}}$ s [40]. This confirms the result obtained in the present work.

The half-life is important for the calculation of the Gamow-Teller matrix element form factor c_{1h}. The value 0.253 ± 0.004 comes from a calculation where the $logft$ value of ^{20}F was 4.9753 [11]. The $logft$ value was averaged with the $logft$ value of ^{20}Na, and have the difference of the two values was taken as an error bar. Taking the f value from Genz [36], the $logft$ value using the current half-life result is 4.9710. This would bring the average value of the $logft$ values down from 4.983 to 4.980. This would then move the value of c_{1h} to 0.254, which is still within the error bar. The new value of the half-life therefor has a negligible effect on the extraction of the Fierz term.

Several things about the data set were discovered. It was learned that there were contaminants coming from the fragmentation of the ^{12}C in the plastic scintillator. It was also

discovered that the rate dependent gain effect in the CsI(Na) implant detector is significant. Before doing this measurement, it was assumed that the low rates would make that effect negligible. It was learned that after the coincidence, the amount of background left in the spectrum is negligible, and that we have no contaminants in the beam.

Chapter 7

GEANT4 Monte Carlo

After the half-life measurement was completed, the next step was to fit the beta energy spectrum for the Fierz term. The corrections to the phase space were the first part of describing the energy spectrum. The effect of bremsstrahlung and the efficiency of the detectors needed to be simulated. The absorption of the 1.6 MeV gamma ray needed to be accounted for. The way this was done was with a GEANT4 simulation [41]. The most updated copy of the code can be found at https://github.com/maximilian29631/Geant4for20F/.

7.1 GEANT4 Inputs

The phase space energy spectrum multiplied by the corrections was fed as input to a Monte Carlo. The program used to model the detectors was GEANT4 version 10.04.02. In order to use the program, the detector geometries were needed.

7.1.1 Detector Geometry

The detector geometry was taken from the technical drawings of detectors. A drawing of the CsI(Na) implant detector is shown in figure 7.1. Based on this figure, the geometry of the detectors was programmed into the simulation. The implant detector was a $54 \times 54 \times 101.6$ mm^3 prism of CsI. Around the prism there was an empty layer. Along the sides, the

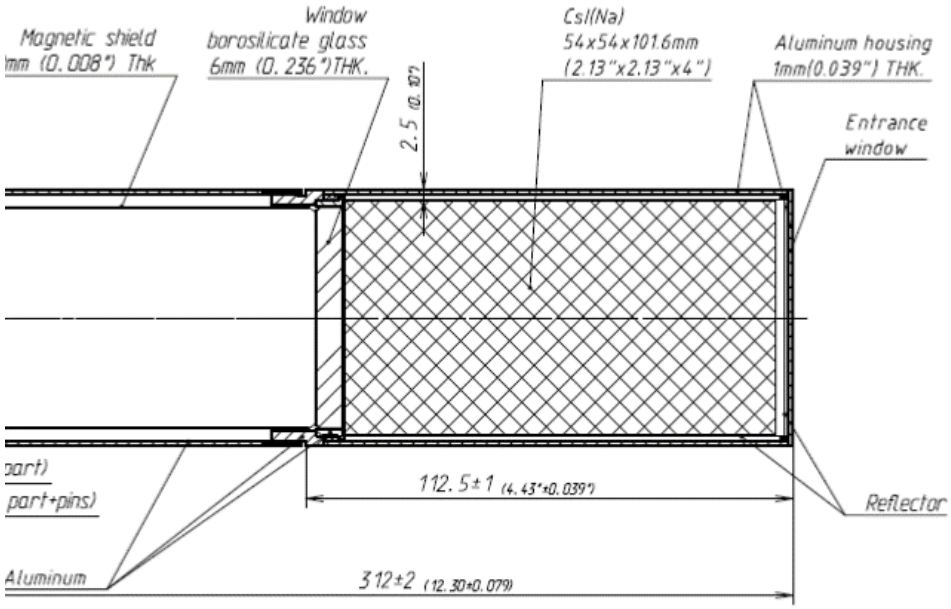

Figure 7.1: A technical drawing of the CsI(Na) implant detector.

empty layer was 1.5 mm thick. On the front and back of the detector, the empty layer was 3.64 mm thick. After the empty layer, a 1 mm aluminum can surrounded the detector on all sides. The nature of the material indicated as "Reflector" was checked with the manufacturer (Scintitech). This material does not cover the empty layer as suggested by the drawing and was confirmed by the implantation depth measurement, which is seen in figure 4.3. The center of this detector was placed with a 4 mm vertical offset of the center of the simulation.

The four large gamma detectors are also square prisms. The active volume was 79.5 × 79.5 × 76.2 mm of CsI. An empty layer was added to the gamma detectors. The empty layer on the sides was 1.5 mm thick. On the front, however, the empty layer was 2.92 mm thick. On top of this, the can of aluminum, 1 mm thick on all sides of the detector was added. The four detectors were arranged in a cross. The detectors were oriented in such a way that

the square face of the CsI crystal faced the implant detector. The edge of each of the large gamma detectors was placed 25.4 mm away from the front edge of the implant detector. This modeled how the implant detector was recessed in the experiment. A visualization of the CsI crystals in GEANT4 is shown in figure 7.2.

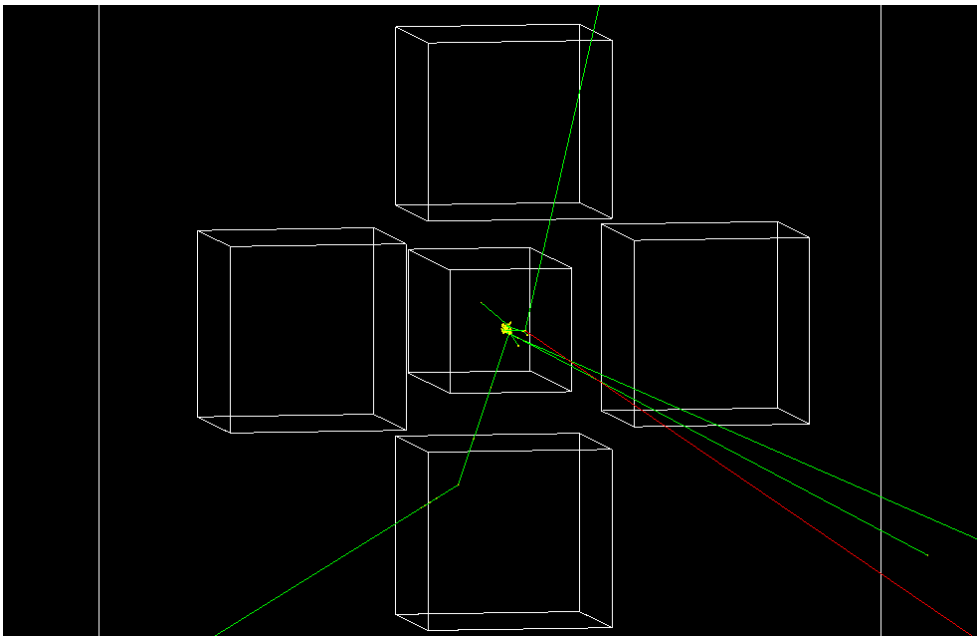

Figure 7.2: The detector geometry inside GEANT4.

7.1.2 Source Definition

The next step was to define a region inside the implant detector. This region was where the primary particles originated from. The depth of the region was calculated using LISE++. As explained in section 4.2.1, the vertical and horizontal size of the region was calculated by using the PPAC measurement and an ion optics simulation. This size was 0.4 × 3.5 × 3.6 mm. The source was implanted 11.56 mm from the front edge of the detector.

7.1.3 Primary Particle Definitions

There were three primary particles generated. Two were photons and one was an electron. All three particles had an isotropic angular distribution. The first particle was an electron. This selected the point in the source region. In order to generate the correct energy for this electron, the following process was used. First, all the corrections described in chapter 3 were multiplied with equation 3.5. This resulting function was evaluated at 1024 evenly space points from 8 keV to the end point energy. This list of 1024 points was fed into GEANT4 as a histogram, as GEANT4 can only take a histogram of up to 1024 bins. Linear interpolation was used to sample this histogram. The interpolation was tested and was found to reproduce the beta spectrum.

The next particle was the 1.6336 MeV photon from the ^{20}F decay. This initial photon was monochromatic and isotropic. The photon started from the same vertex as where the electron was generated.

The last photon was to account for the inner bremsstrahlung. The radiative correction used to generate the electron energy was the formula that assumes all real photon energy is absorbed (equation 3.9). After the electron energy is generated, the formula describing the energy spectrum of the inner bremsstrahlung photons is generated. This spectrum is written out in equation 3.10. A cutoff of 50 keV is imposed to the formula. Then, the formula is numerical integrated from 50 keV to the electron energy over 1000 steps using the trapezoidal rule. This is the total probability that an electron emits an inner bremsstrahlung photon. This number is compared to a random number from 0 to 1. If the random number is below the integral, the inner bremsstrahlung energy spectrum is sampled. The algorithm used for this sampling is the von Neumann method [42]. The sampled energy is given to the

third primary particle. If the random number is more than the integral, the third primary particle is given an energy of 0 keV. The energy of the electron is reduced accordingly.

The two photons had their initial points moved to match that of the electron. All three particles were then free to propagate through the detectors.

7.2 Particle Propagation

GEANT4 propagates the particles in steps. During or after each step, different physics processes are carried out. The physics process may create secondary particles. If these secondary particles cannot make it the length of the range cut, they will not be created. These cuts can be set differently for different particles. The range cuts correspond to a threshold of 15 keV in aluminum. These steps happen until the primary particle runs out of energy.

7.3 Simulation Output

The particles were tracked and the energy deposited in each detector summed up. The energies deposited into the implant detector was summed up into two categories. The energy deposited from the initial gamma ray was one category. The other was the energy deposited from the initial electron. After the energies of the particles reached a certain threshold, the simulation of one decay was finished. All the energies deposited into each of the detectors was summed up and saved as an event in a ROOT TTree. Then, the process was repeated. A new location inside the region was generated and another decay generated.

For the fit, four different simulations had to be run. Each of them needed 1.4×10^{10} events in order to have 100 times the total in the data. To test the systematic effects, only

2×10^9 events were run. In order to decrease the time it took to run, the range cuts on the gamma rays were changed. The range cuts were changed from 5 μm to 1 mm for gamma rays. The range cuts for other particles stayed at 5 μm.

7.4 Simulation Development

The GEANT4 simulation is based on the example TestEm5. The first changes were in the detector geometry. The next changes were to add a second primary particle, which was the gamma ray from the decay. The data structure that recorded all the data absorbed event by event was added, so that the gamma cuts could be changed after the fact.

Initially, all energy absorbed by the implant was recorded, regardless of its origin. This was found not to be the correct way to fit the data, so the class G4VUserTrackInformation was implemented. This gave to each track the information about the primary particle. To split the energies from different detectors, the initial energy and charge of each primary particle was checked. Since the gamma rays are monochromatic, the energy of the primary particle was compared to 1.6336 MeV. If the primary particle had charge or it was a photon without an initial energy of 1.6336 MeV, it was put in the category of energy from the initial electron. This took care of most cases, unless a sampled inner bremsstrahlung photon had exactly that energy, which was rare enough to be negligible.

The radiative correction used was changed. Initially, it was assumed that all the real photons generated by the radiative correction would be absorbed. It was also assumed that the higher energy inner bremsstrahlung would not come in large enough numbers to have an appreciable effect. This would make the radiative correction in equation 3.9 adequate. However, after explicitly generating the inner bremsstrahlung photons, this was found not

to be true. Therefore, the entire simulation had to be rerun with the inner bremsstrahlung photons generated explicitly.

Then, it was discovered that only running one simulation was not the correct way of fitting the data. Initially, the corrected phase space without the shape factor was fed into the GEANT4 Monte Carlo. Then, during the fitting, the shape factor multiplied the output. This mixed the initial energy of the electrons with the energy absorbed by the detector, which are not the same. This is not correct, and four simulations were needed. The simulations were the phase space times the pieces of the shape factor. The first version of the code took a week to run 2×10^9 events. This was an issue if four simulations would be needed. To speed up the code, the code was modified to use GEANT4 MPI parallelization. The code was then run on the fireside cluster at the NSCL. After modification, it only took 6 hours to run 2×10^9 events.

7.4.1 Data Output Changes

Another change that was made is in how the simulation results were built. Initially, all the energy absorbed in each detector was put into a TTree. This meant that 2×10^9 events generated 60 GB of output files. To reduce this space requirement, only events were any gamma detector had a non-zero input were first recorded. This cut down the space required by 1/3 to 20 GB. This was not enough, however, as each fit needed four histograms. A requirement that only one detector fired in order to get the event recorded in the TTree was imposed. This cut down the space to 16 GB. As the final simulation needed 1.4×10^{10} events, this still was not enough. The lesser amount of events was used to test the fit method and calculate systematic effects.

Since there is a requirement for only one gamma detector to absorb energy, the gamma-

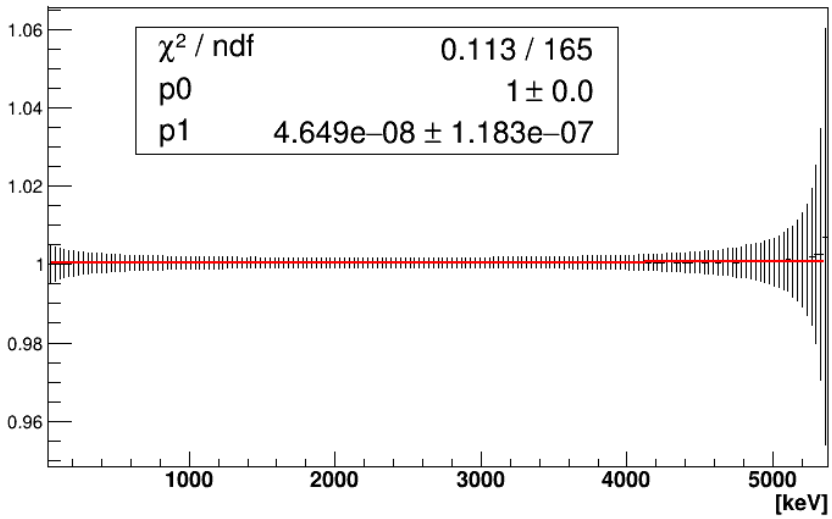

Figure 7.3: Ratio of processing data two different ways. This is all the energy absorbed in the implant detector.

beta coincidences are independent detector to detector. To save space, it is then possible to build 2-D histograms for each of the four gamma detectors. The energy of the gamma ray was plotted on the x-axis, and the energy absorbed in the implant detector on the y-axis. For each detector, two of these histograms were built. One had the beta-only information. The other had the information about the beta-gamma sum spectra. Then, when it came time to apply the beta cuts, the 2-D histogram was projected onto the x-axis and the spectra built. To check if the binning applied to the histogram distorted the output spectra at all, ratios of the two output spectra were taken. The results of the ratios can be seen in figure 7.3. The red line fits the ratio very well. The relative normalization *p0* is consistent with 1, which means both spectra have the same number of counts. The slope *p1* is consistent with zero to 10^{-7}. This is much smaller than the linear term in the shape factor. From this, it is seen that processing the data differently has no effect on the outcome. This method of processing the data was used to test the sensitivity of the fit to the charge radius and the beta end point.

Chapter 8

Fitting Beta Spectrum

The output of the GEANT4 simulations was used to fit the beta spectrum for b_{WM} and b_{GT}.

8.1 Fitting Method

Four GEANT4 simulations were used for the fit. The fitting function includes the phase space, corrections, shape factor, and Fierz term and can be written as

$$\frac{dN}{dE} = PS(E) \times C(E) \times (1 + c_0 + c_1 E + c_2 E^2 + \frac{c_{-1}}{E}) \times (1 + b_{GT}\frac{m_e}{E}) \tag{8.1}$$

with $PS(E)$ being the phase space, $C(E)$ the corrections, the c_i the terms of the shape factor, and E the total electron energy. The $PS(E) \times C(E)$ can be distributed to the shape factor, and four terms appear. Since the c_i and b_{GT} are small, $b_{GT} \times m_e$ can be, to first order, added to c_{-1}. These four terms are the inputs to the GEANT4 simulation. These are summarized in table 8.1.

Table 8.1: The four histograms used for the fits.

Name	Formula	Normalization (when E is in keV)
$f(E)$	$PS(E) \times C(E)$	1
$g(E)$	$PS(E) \times E \times C(E)$	3.35e-4
$h(E)$	$PS(E) \times E \times E \times C(E)$	9.89e-8
$j(E)$	$PS(E)/E \times C(E)$	2494

Each of these pieces was generated with the same number of events. Due to the different shapes of the spectra, a relative normalization was required. The normalization was determined by taking the ratio of each the input spectrum of each piece compared to $f(E)$ and fitting it with the relevant power of E. These four pieces were the inputs to the GEANT4 simulation.

8.2 Simulation Results Processing

In order to use simulations results for fitting, further process had to be done in order to build the histograms for the fitting of data. The TTrees or histograms in the output of the simulation was used. First the detector response of the gamma detectors was applied. The procedure for doing this is described in section 8.2.1. The energy absorbed in the implant detector was filtered by the energy absorbed in the outer four gamma detectors in the simulation. The energy gate was adjusted to match the energy gates of the data, which was the same as in the half-life measurement in table 6.2. The energy gates were converted to keV using equation

$$C = G \times E + b \tag{8.2}$$

where C is the location of the peak in ADC channels, G the gain in ADC channels/keV, and b the offset in channels. The values of the parameters for gamma detector calibrations and response are summarized in table 8.2.

The two different categories of energy absorbed in the implant detector were built into two histograms. One histogram had a condition that the energy deposited by the initial gamma ray had to be zero. This histogram was the energy absorbed without any summing. The second histogram was the energy absorbed where there was a contribution from the

Table 8.2: The values of the calibration parameters using the gamma sources.

Detector	Gain (ADC Units/keV)	Offset (ADC Units)	Convolution constant ($keV^{1/2}$)
Up	0.90	28	1.25
Left	0.86	20	1.26
Down	0.96	27	1.19
Right	0.97	23	1.18

gamma ray in the implant detector. This histogram was known as the beta-gamma sum spectrum. These two histograms can be seen in figure 8.1.

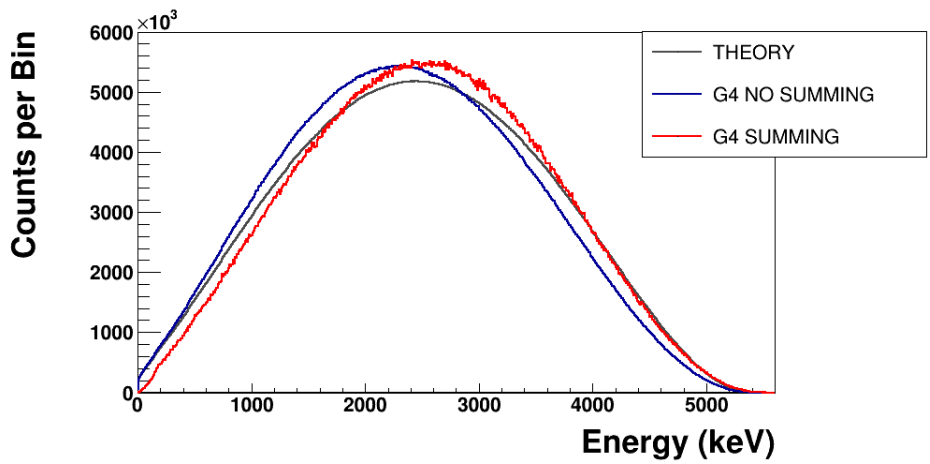

Figure 8.1: The shapes of the different histograms from the output of the GEANT4 simulation. The input beta spectrum is also plotted. The histograms are scaled to the same maximum.

Another set of histograms was built with different gamma conditions. To build the new gamma conditions, the ADC unit difference between the upper and lower gamma cuts was taken. This was added to the old upper and lower gamma cuts to get the new gamma cuts. The new gamma cuts were to match the data background cuts, which are shown as the red lines in figure 8.2. Then, the simulation was filtered through these new cuts to build a background spectrum. This background GEANT4 spectrum was subtracted off of the signal spectrum. This procedure was done for all four histograms needed for the fitting procedure. The next thing to do was to apply the detector response.

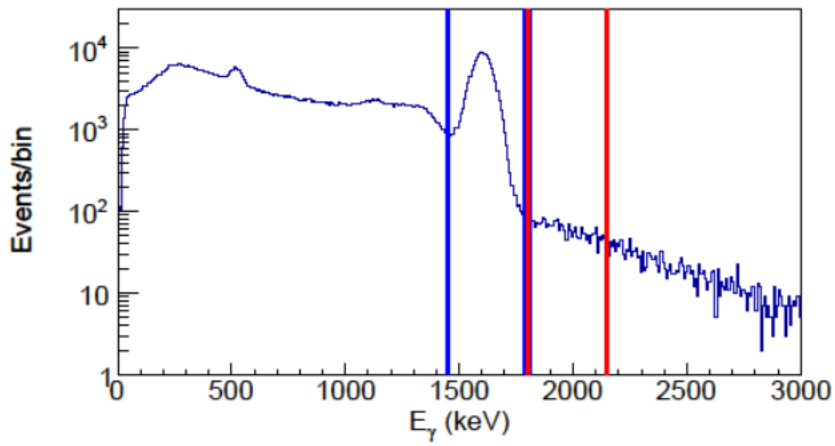

Figure 8.2: A sample gamma spectrum showing the position of the gamma cuts used to build the beta spectrum. The blue lines show the cuts used to build the signal spectrum. The red lines show the cuts used to build the background spectrum.

8.2.1 Detector Response

Accounting for the detector resolution was done by applying a convolution function to the histograms built from the GEANT4 output files. The convolution function was a Gaussian function. The σ of that Gaussian function depended on the energy as

$$\sigma(E) = A\sqrt{E} \tag{8.3}$$

where σ was the standard deviation and A a constant found through a calibration. This was done by looping through each of the histograms' bins and reading the number of counts in each. Then, a Gaussian distribution was built for each bin. The center of the Gaussian was the center of each bin in keV. The σ of the Gaussian was calculated by using equation 8.3. This Gaussian distribution was sampled as many times as there were counts in the bin. These samples were filled into a new histogram. This was repeated until all bins were distributed. This was done separately for each of the four spectra.

8.2.1.1 Determining Detector Response

In order to properly fit the energy spectrum, a calibration of the CsI(Na) detector had to be done. The calibration was used to find the value of A in equation 8.3. Several different energy lines were used. The lines were the 1.173 MeV and 1.332 MeV gammas from a ^{60}Co source, the 0.662 MeV gamma ray from a ^{137}Cs source, and the 0.511 MeV and 1.274 MeV gamma rays from a ^{22}Na source. These gamma rays were fit with a Gaussian and a background. The background varied from no background, a linear background, a quadratic background, and an error function background. For the ^{60}Co, both peaks were fit at once. These different background gave slightly different results for the centroids and the widths of the Gaussian. The range of the centroids and widths was taken as a systematic error. From the centroids, the calibration for each detector was calculated with equation 8.2. The widths of the peaks were calibrated with the gain and plotted vs energy. Then, equation 8.3 was fit to the results in order to determine A. The value of A used for this procedure was 1.112 with an uncertainty of 0.008. After applying the detector resolution, the pile-up in the detector had to be modeled.

8.2.2 Pile-up Modeling

In order to model the pile-up properly, a model of the detector pulses was needed. For the CsI(Na) signals, a linear rise and then an exponential decay was used. The linear part went from 0 to 1 over 100 ns. The exponential piece started at 100 ns at 1 and decayed with a decay constant of 760 ns. This analytic equation was scaled up or down to whatever energy was sampled. It was then fed into a model of trapezoidal filter of PIXIE. The sums shown in equation 5.1 were done and the energy calculated.

This model was tuned on calibration data. A spectrum was taken of ^{137}Cs at 25000 counts per second. A ^{137}Cs spectrum taken at 2000 counts per second was used as a background and subtracted off. Then, samples of the background-subtracted spectrum were taken up to the end of the 661 keV peak. Monte Carlo methods were used to model the time difference between two samples. If the two samples fell within the pile-up window, then the piled-up signal models were fed into the trapezoidal filter. The calculated pile-up energy was saved to a histogram. If the two samples did not fall with in the pile-up window, then they were not fed into the filter model and just filled into the histogram. The parameters were adjusted until the generated pile-up matched the measured pile-up in the spectrum. The results of the tuning is seen in figure 8.3.

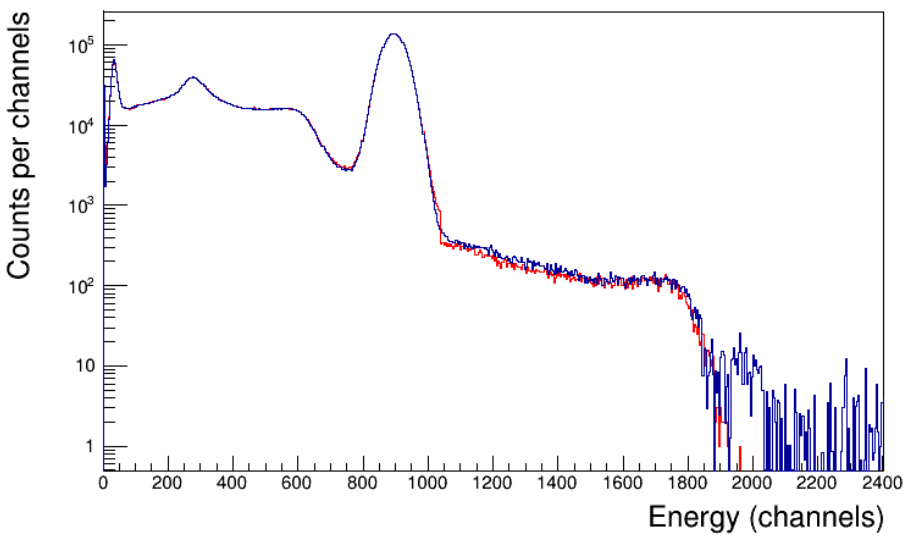

Figure 8.3: The tuning of the pile-up. The input spectrum is in blue. The generated spectrum is in red. The red spectrum was generated from sampling the blue spectrum up to energy 1000 channels. These samples were put through the pile-up model.

For the pile-up model, the resulting times are shown in table 8.3. In addition, the parameters of the actual energy for the CsI(Na) implant detector are shown.

The τ value in the pile-up tuning is very similar to that of the energy filter. The other

Table 8.3: Pile-up model parameters compared to the energy filter parameters.

Parameter	Pile-up model value	Energy filter value
τ	880 ns	900 ns
$t_{PEAKING}$	880 ns	480 ns
t_{GAP}	72 ns	48 ns

parameters are roughly double in the pile-up model compared to that in the PIXIE energy filter.

The pile-up model was applied to the simulation after the detector response was applied. Of the four different simulations needed for a fit, only $f^*(E)$, $f(E)$ after applying the detector response, was fed into the pile-up model. The amount of pile-up is small. Applying the pile-up to the other terms of the shape factor gives a negligible contribution. The beta only spectrum and the beta-gamma sum spectrum of this simulation was added together and fed through the pile-up model. With the pile-up spectrum described, all the pieces of the fit function are in place.

8.2.3 Fit Function

For the fit function, the convoluted histograms and pile-up were rebinned to a bin width of 32 keV. Then, each of the histograms were turned into a spline. The five splines were fed into a fit function. The fit function was

$$H(E) = A \times [(1+c_0)f^*(E) + c_1 g^*(E) + c_2 h^*(E) + (c_{-1} + b_{GT} m_e) j^*(E)] + B \times pu^*(E) \quad (8.4)$$

where A is the normalization, B the level of pile-up, $pu^*(E)$ is the generated pile-up spectrum, and $f^*(E), g^*(E), h^*(E)$, and $j^*(E)$ the different simulation histograms shown in table 8.1

after the convolution was applied. In order to change the units of the x-axis in the data to energy in keV, a calibration was needed. For this calibration, the offset was fixed in the fit function. However, the gain of the calibration was left as a free parameter. This was to account for gain shifts, such as an apparent rate-dependent gain shift due to the afterglow in the crystal.

In the fit, each of the c_i were written out in terms of the nuclear form factors. In these form factors, b_{WM} was left as a potential free parameter. If b_{WM} was fit with the fit function, b_{GT} was fixed to be 0. If b_{GT} was fit, then b_{WM} was fixed to be 43.4. In total, the fit function had four free parameters: A, B, the gain G, and either b_{WM} or b_{GT}. In order to benchmark this fitting method, pseudo-data was generated and fit.

8.2.3.1 Fit Function Characterization

Different methods of the fit function were tested. The first is the so-called "hybrid method", where only one simulation is needed. The GEANT4 with only the phase space and corrections is generated. Then, it is multiplied by the shape factor. This function was

$$H^*(E) = A \times f^*(E) \times S(E) + B \times pu^*(E) \tag{8.5}$$

with $S(E)$ being the shape factor. This method of fitting is not correct, as the E in $f^*(E)$ is not the same as the initial energy in the analytical shape factor $S(E)$.

The first test was done just with a linear term in the pseudo-data. An older version of the GEANT4 code had a phase space times corrections times a linear shape factor fed into it. This pseudo-data was fit with the hybrid model. Initially, the shape factor was applied to the total energy inside the implant detector. This was found to induce a shift of the

measured linear term. Applying the shape factor only to the beta only part of the spectrum solved this issue.

To further test the fitting method, two more spectra were generated. One had the nuclear shape factor with $b_{WM} = 43.4$, which was the new pseudo-data spectrum. The other had no shape factor. After applying the coincidence condition to both of these simulations, the function with no shape factor was used to fit the function with the shape factor. The gain in these fits was left as a free parameter, and the offset was fixed to a value of 0. To manually check the statistical uncertainty, the pseudo-data spectrum was fluctuated. Each bin had its content and error read. That bin error and content was used to build a Gaussian random number distribution. This random number distribution was sampled, and a new bin center created. After doing this to the entire spectrum, the new spectrum was fit. The resulting b_{WM} was recorded. Then, b_{WM} was set to 43.4, and the Fierz term fit. These fit terms were saved to a histogram. This was done 1000 times to get a spread of values. From this, it was discovered that spline interpolation was the best way to fit the spectra.

The same method was used to see if the fit result was sensitive to the lower limit of the fit interval. 1000 spectra were generated by scrambling one spectrum over and over. These spectra were fit from a lower beta cut up to the end point minus 100 keV. The lower beta cut was varied from 200 keV up to 2 MeV. From this it was found that this fitting method gave inconsistent results above 1200 keV. This effect was very large in the extraction of b_{GT}.

Doing the same thing with the four-histogram fitting method described above showed that there is not such a sensitivity. The four histogram fit is the one described above. More pseudo-data was generated, along with four histograms to be used for fitting. This was largely done to get a handle of the normalization of the histograms. The normalization was obtained by taking the ratios of the histograms and fitting them with the functional forms.

After the normalization, the fit was done. The output b_{GT} and b_{WM} obtained from the fits of the pseudo-data was the one put in.

8.3 Experimental Data Processing

After the fit function was tested and verified, the data was ready to be fit. For the fit, the experimental data had to be filtered as well. The energy spectrum of the implant detector was put in coincidence with the 4 gamma detectors. The energy cuts of the gamma detectors were the same as in the life-time measurement, as seen in table 6.2. An additional condition was that only one of the gamma detectors could have fired for each event, much like the processing for the GEANT4 events.

A different condition in the data was on the time difference. For this measurement, the time difference between a beta event and a gamma event had to be between -300 and 24 ns. This captures the entire spectrum, as the time stamps are strongly dependent on energy. Then, a 2-D histogram was built, with energy on one axis and time since last beam-on on there other. The decay cycles were 22 s long for the CsI(Na) implant data and were split up into 3 segments with equal number of counts. To do this, it was assumed that the rate depended on the time as an exponential with a half-life of 11 s. The time interval was split in such a way that the integral of the exponential was equal over the 3 different segments. The total time interval was from 1.5 to 22 s. These splits worked out to be at 5.89 s and at 11.98 s. This 2-D histogram was projected onto the energy axis between the splits in order to build the energy spectrum of the fit.

8.3.1 Background Subtraction

A background subtraction of the data was required. To build the background, cuts placed above the regular gamma cuts in table 6.2 were used. Much like in the processing of the simulation spectra, the difference between the upper and lower gamma cuts were taken. These differences were added to the original upper and lower gamma cuts to get new gamma cuts. A beta spectrum was built with a time difference condition and these new gamma cuts. This was the background spectrum. It was then subtracted off of the signal spectrum. The position of the gamma cuts on a sample spectrum is shown in figure 8.2.

8.4 Beta Spectrum Fit Procedure

After the data was processed, the fit was done run by run. First a prefit for each section was done to calibrate the energy from 500 channels to 6000 channels. This was done to obtain a calibration of the data. Then, two endpoints fixed in keV were used for the actual fit. The fitting function with a fixed offset was fit using a maximum likelihood method. The value of b_{GT} was fixed to 0, and the resulting b_{WM} was recorded. Due to the anti-correlation between b_{WM} and b_{GT}, only one parameter at a time could be fit. For the Fierz term fit, the $b_{WM} = 43.4$ was applied to the shape factor and the b_{GT} was recorded.

The offset used for the fit was varied. The effect of the offset will be discussed in the next section. The calibrated start and end of the fits were 250 keV to 7500 keV. A sample fit is shown in figure 8.4. The spread of values from the fits can be seen in figure 8.5. Fitting the resulting values of b_{WM} with a constant gives $41.0 \pm 1.7_{\text{stat}}$ with a χ^2/NDF of 70.4/56. Since the χ^2/NDF is greater than 1, the statistical uncertainty was multiplied by $\sqrt{70.4/56}$ to give 1.9. Similarly, fitting the resulting values of b_{GT} with a constant gives $0.0021 \pm 0.0041_{\text{stat}}$

with a χ^2/NDF of 86.4/56. Multiplying the statistical uncertainty by $\sqrt{86.4/56}$ gives 0.0051.

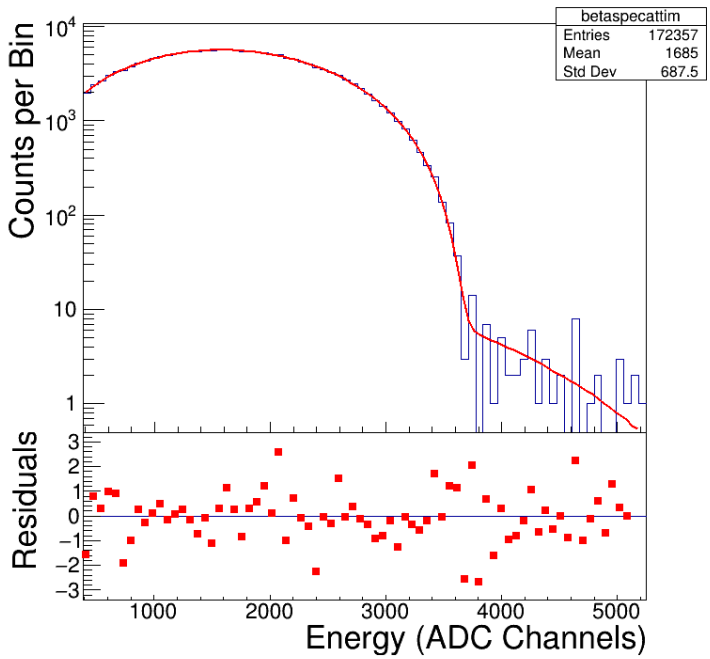

Figure 8.4: A sample fit of the beta spectrum. The residuals of the fit are shown below the graph. The χ^2/NDF of this fit is 175.4/151.

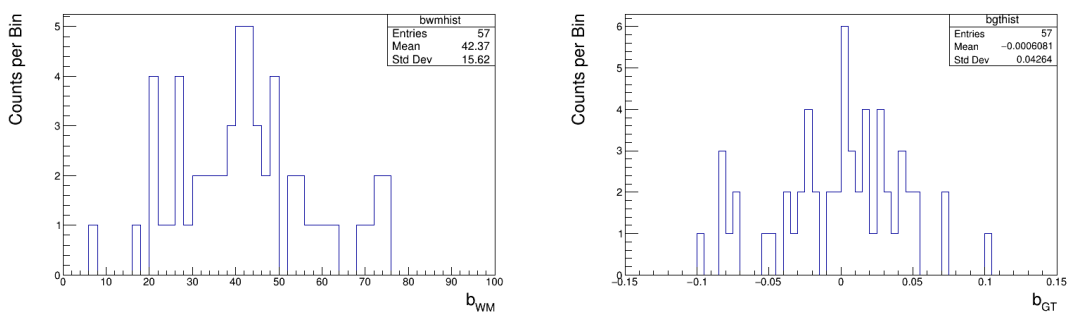

Figure 8.5: Histograms of all the results from the fits. These graphs do not account for the uncertainties in each fit

8.5 Systematic Uncertainties

After testing the fit and fitting the data, the systematic effects were investigated. The systematic uncertainties can be divided into three categories. The first are the uncertainties

that have to do with the inputs to the simulation. The second has to do with the inputs to the fit. The final has to do with the uncertainties of the nuclear form factors in the shape factor. One of the largest systematic uncertainties has to do with the position where the fit is started.

8.5.1 Lower Beta Cut Sensitivity

The lower beta cut sensitivity is the systematic shift of the fit gain G as a function of where the fit started. If these are incorrect settings, b_{WM} and b_{GT} get correlated with G and shift as well. There are several different input factors that can induce such an trend. Plotted in this section is the average gain from the b_{WM} fit, G_{SM}, and the average gain from the b_{GT} fit, G_{BSM} obtained from the 57 individual fits.

8.5.1.1 The Offset

Initially, the used offset was the offset from the calibration in equation 8.2. The offset used was 10.05 ADC units. This calibration was determined using photons instead of electrons. It also doesn't probe the same location as where the beta electrons are.

When applying an offset of 10.05 in a fit of the data, it was found that the output varied greatly as a function of where the fit was started. For these graphs, the end of the fit (or upper beta cut) was set to 7500 keV. The detector is known to be non-linear below 200 keV [43], so any fit starting below that point is suspect. After 2000 keV, the shape of the beta spectrum makes getting a good fit unlikely. The lower beta cut was varied between these two end points. The effect in the average gains is shown in figure 8.6.

To test the effect of the offset, a Monte Carlo was written. A sample histogram with only the phase space and the shape factor was generated. These histograms were generated

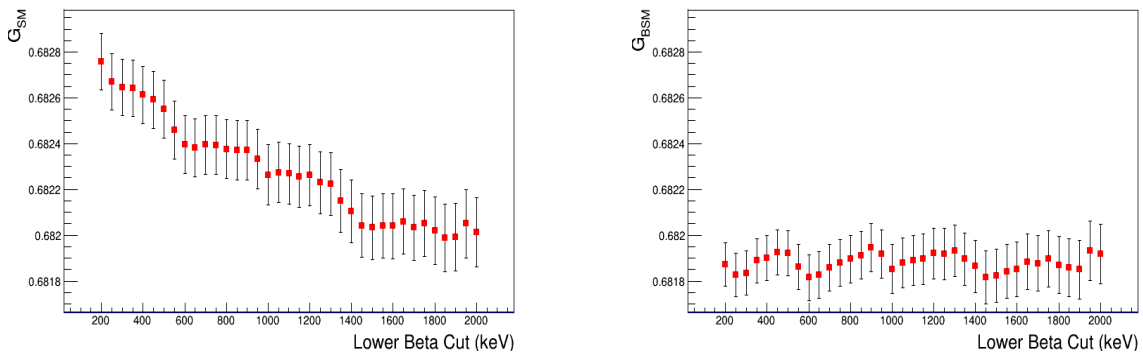

Figure 8.6: For the standard model fit, there is a large dependence of the gain on the start of the fit. The offset here is 10.05.

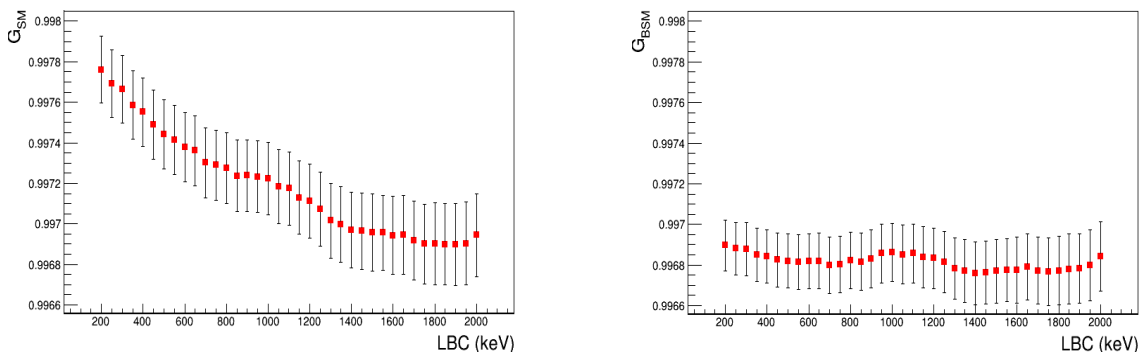

Figure 8.7: This is Monte Carlo data. The curves were generated with an offset of 0 and fit with an offset of 15. A trend similar to that in the data is seen.

with an offset of 10 ADC units. A random gain was applied to the pseudo-data histogram. Then, the fit function had a different offset applied to it. For example, fitting the histogram generated with an offset of 0, and fit with an offset of 15 gives an effect as seen in figure 8.7. In the Monte Carlo, this fit resulting with a gain shift of 6.2×10^{-4} from 200 keV to 2000 keV. In the data, this shift is 5.0×10^{-4}. In addition, in both the data and the Monte Carlo, the trend is only seen in the G_{SM} fits.

This effect can be exploited to determine an offset using only the data. The size of the slope induced is linear compared to the offset. By adjusting the offset and noting the slope of the G_{SM} vs the lower beta cut and plotting against the offset, the location of zero slope can

be calculated. This graph is shown in figure 8.8. The resulting G_{SM} and G_{BSM} curves are

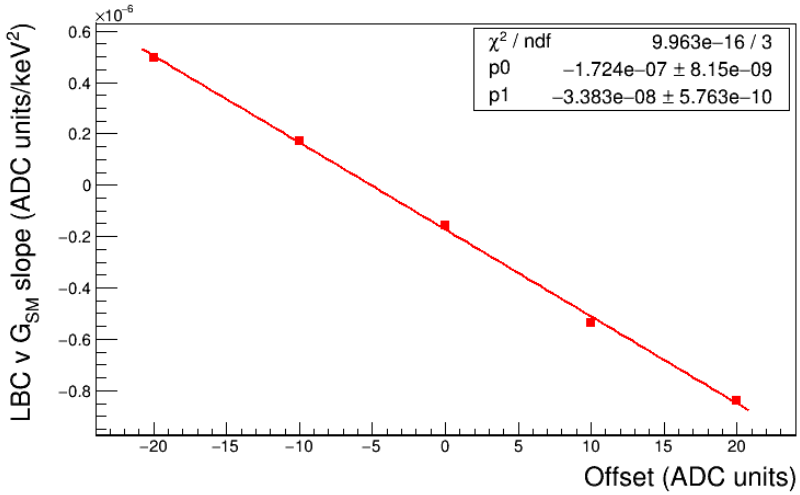

Figure 8.8: How the slope of the G_{SM} vs LBC curve changes with offset. A slope of 0 corresponds to an offset of -5.1.

seen in figure 8.9. The difference between the mean value of G_{SM} and G_{BSM} is 3.8×10^{-5}.

To estimate the uncertainty on the offset, the difference between the fitted gains were plotted vs thee lower beta cut. The offset was changed from -5.1. The point at which the effect induced by the offset overwhelmed the statistical fluctuations was taken as the uncertainty of the offset. This uncertainty was 0.5.

Since gains plotted in figures 8.6 and 8.9 are the averages of the fit gains and there is a

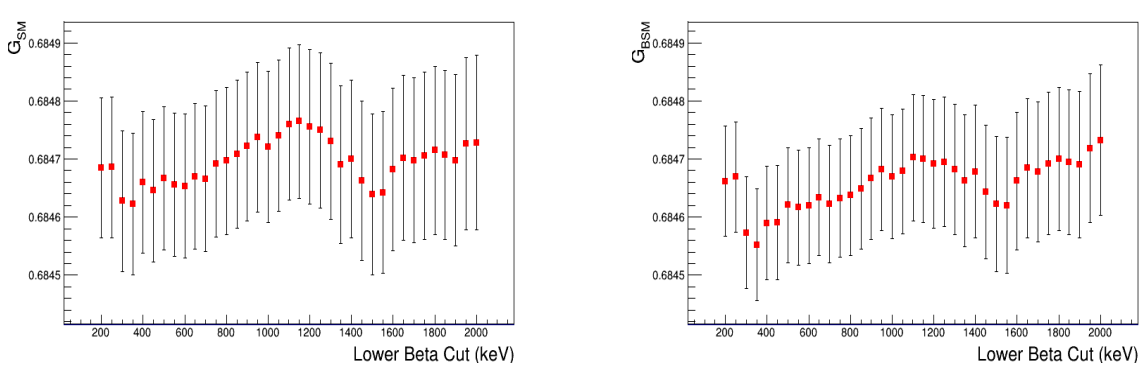

Figure 8.9: The dependence of the parameters to the start of the fit. The offset here is -5.1. Both gains are independent of the start of the fit.

large global gain shift from run to run, other effects could be important.

8.5.1.2 The Convolution

Another potential effect is if the detector resolution was applied incorrectly. To test that, a Monte Carlo simulation was written. The phase space in equation 3.5 was multiplied by the shape factor in equation 3.26. This function was sampled 10^9 times twice to build two histograms. Both histograms had a detector resolution applied as described in section 8.2.1 One histogram was sampled a further 10^6 times 10 times to build a sample data set. The other convoluted histogram was used to fit the generated data set. The first histogram's A was fixed, while the second histogram's A was adjusted. When the sample data's A matched the A that were used, no dependence of b_{WM} on the start of the fit was found. When the A of the data sample and the A of the fitting histogram differed, the first thing that happened was that the b_{WM} changed. If the A differ by a factor of 2 or more, a shift in b_{WM} appears. However, this is much larger than any uncertainty in detector resolution, which is estimated to 0.008. The effect of a wrong detector resolution is negligible.

8.5.1.3 The Relative Normalization of the Beta-gamma Sum Spectrum

The relative normalization of the beta-gamma sum spectrum can induce an effect which is seen in the fit gain. This was checked with the same Monte Carlo used to test the effect of the offset. The size of the beta-gamma sum spectrum was increased in the pseudo-data. Then, the fit was done and gain recorded. The lower beta cut of the fit was changed, and the changes in the gains recorded. In order to induce an effect, the size of the beta-gamma sum spectrum would have to be off by a factor of 3. Additionally, this effect would be seen in both G_{SM} and G_{BSM}. Therefore, this effect can be excluded.

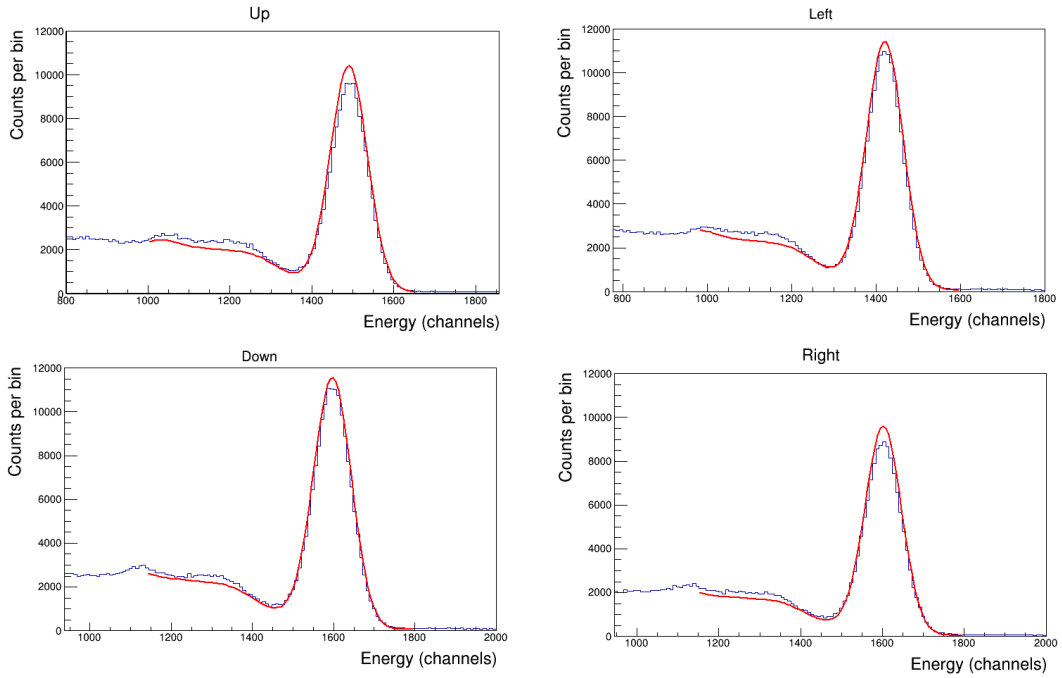

Figure 8.10: A sample fitting of the gamma detectors over the Compton scattering range.

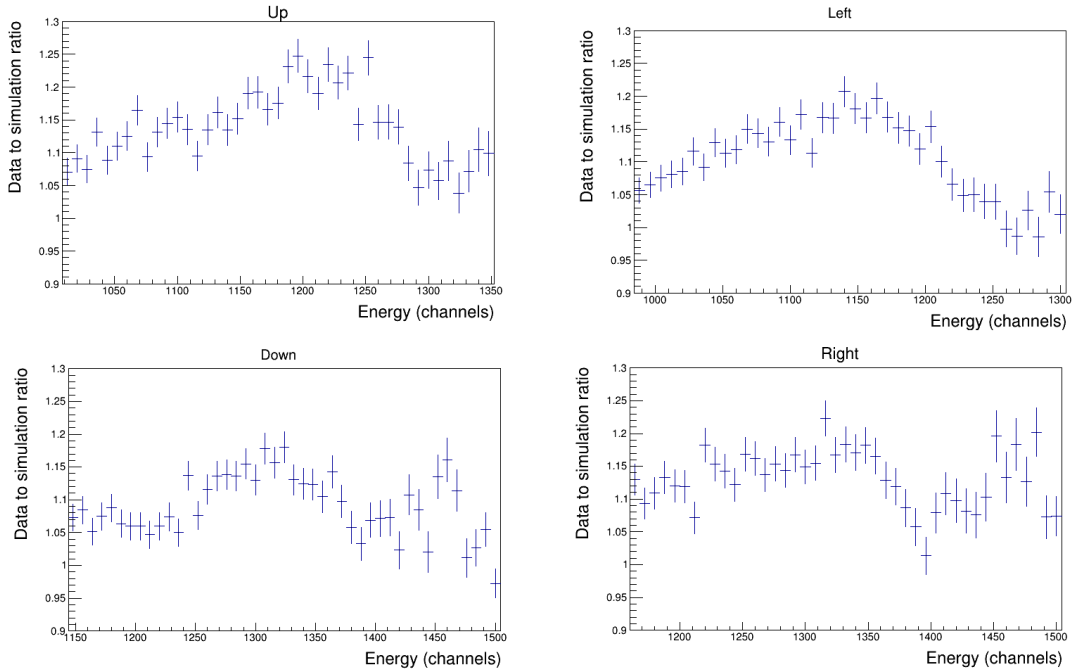

Figure 8.11: The ratio of the data to the fit function in the fits shown in figure 8.10.

In order to get an estimate of the systematic uncertainty on the normalization, sample gamma spectra were fit. The energy absorbed in the gamma detectors in the Monte Carlo

were built into histograms. This histograms had the detector responses of the gamma detectors applied to them. The gamma spectrum was over a range including the main peak. This is seen in figure 8.10. GEANT4 overestimates the main peak relative to the Compton scattering region. Since the GEANT4 spectrum, the red line in figure 8.10, is always above the data, there is no issue with the description of the detector response of the four gamma detectors. This was checked by fitting around the gamma peak and seeing a good match. A ratio of the data to this fit was built over the Compton scattering region, which is seen in figure 8.11. This is where gamma detector energy is more sensitive to the relative size of the gamma-beta sum spectrum. The ratio is within 20% for all four detectors, so this was taken as a conservative estimate of the uncertainty in the normalization.

8.5.2 Upper Beta Cut Sensitivity

There is no sensitivity of the result on where the fit ends. An issue is that at small enough upper beta cut, there is nothing to fix the pile-up parameter on. This means that there could be correlations induced. To avoid this, the prefit was done, and the level of pile-up recorded. The level of pile-up was fixed for the other fits across all upper beta cuts. The lower beta cut was fixed to 250 keV in the fits. The effect is shown in figure 8.12. Both parameters are flat after 5500 keV.

8.5.3 Summary of Systematic Uncertainties

For the calculation of the systematic uncertainties, one parameter at a time was changed. The parameter was increased by one unit of the error on that parameter. The fit was redone with the different parameter values. The output b_{WM} and b_{GT} for the changes in the

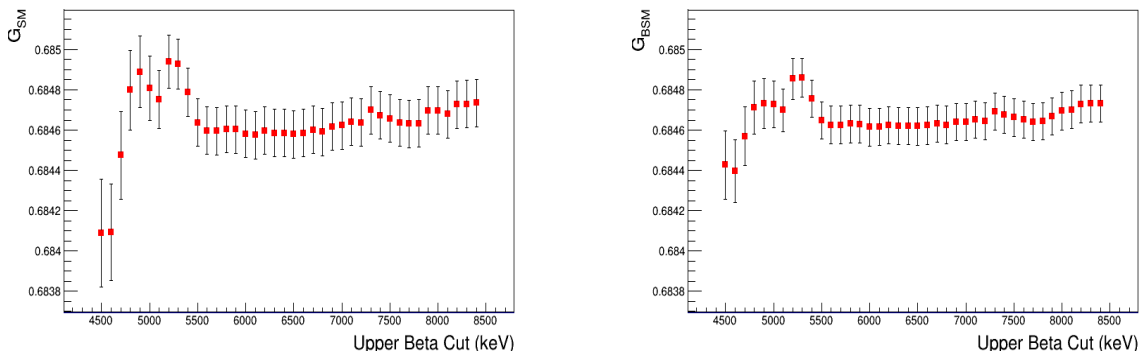

Figure 8.12: The effect of changing the upper beta cut.

parameters were recorded. The parameter was then decreased by one unit of the error. Half the difference of the output b_{WM} and b_{GT} was the systematic error.

As stated above, the different systematic uncertainties can be divided into three different categories. There are the systematic uncertainties due to the simulation inputs, which are summarized in table 8.4. These were all calculated by running the four histograms with 2×10^9 events each.

Table 8.4: Systematic uncertainties due to simulation inputs.

Parameter Name	Parameter Value	Parameter Uncertainty	Systematic Uncertainty b_{WM}	Systematic Uncertainty b_{GT}
Electron maximum total energy	5900.864 keV	0.081 keV	0.2	0.0012
RMS charge radius	3.0055 fm	0.0021 fm	0.2	0.0003

The uncertainty due to the average mass M_{ave} was ignored. The value of the average mass used is 18621497.033 ± 0.040 keV. Since this value appears in the denominator, and the uncertainty is so small, the effect of the uncertainty due to this average mass value is negligible. On the other hand, an uncertainty in the end point can have a larger effect.

The systematic effects due to the fit inputs are shown in table 8.5.

Table 8.5: Systematic uncertainties due to fit inputs.

Parameter Name	Parameter Value	Parameter Range or Uncertainty	Systematic Uncertainty on b_{WM}	Systematic Uncertainty b_{GT}
Relative normalization of the beta-gamma sum spectrum	1	0.2	2.7	0.0063
Binning of data histogram	32	16 to 64	0.6	0.0003
Binning of fitting histograms	32	16 to 64	0.2	0.0007
Offset	-5.1	0.5	1.4	0.0047
Convolution	1.112	0.008	0.3	0.0004

Lastly, there are the systematic uncertainties due to the form factors inside the shape factor. To calculate these systematic uncertainties, two fits one after another were done. First, b_{GT} was fit with the central value of b_{WM}. The resulting gain was recorded. This gain was fixed, and the altered value of b_{WM} applied and b_{GT} was fit again. The difference between the fit values of b_{GT} was recorded as a systematic uncertainty. It was found that the systematic uncertainty of b_{GT} due to the uncertainty on b_{WM} depended on where the fit was started. This is due to the functional form of the shape factor and the Fierz term. b_{WM} contributes most to the shape factor in the linear term c_1, which increases as a function of energy. Conversely, the energy dependence of the Fierz term decreases as a function of energy. This is shown in figure 8.13. This is another reason to start the fit as low as possible. These uncertainties for the form factors are summarized in table 8.6.

The largest uncertainty is due to the relative normalization of the beta-gamma sum spectrum. The next two largest uncertainties are of similar size and are the uncertainties due to the weak magnetism form factor and the uncertainty due to the offset.

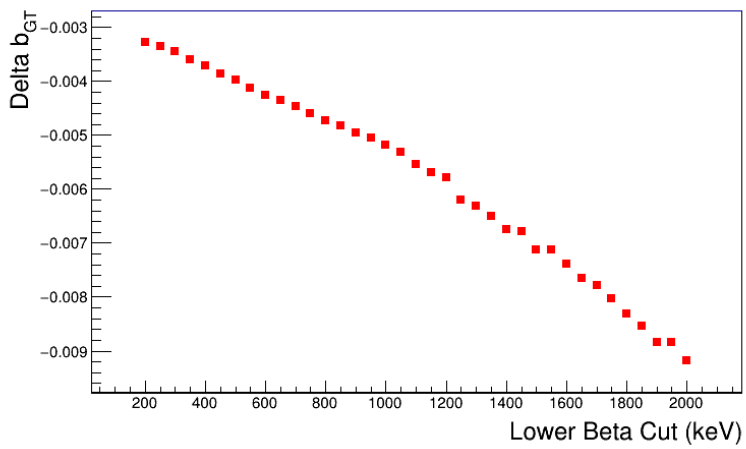

Figure 8.13: This is the systematic uncertainty on b_{GT} due to the uncertainty of b_{WM}. It changes as a function of the lower beta cut.

Table 8.6: Systematic uncertainties due to nuclear form factors.

Parameter Name	Parameter Variable	Parameter Value	Parameter Uncertainty	Systematic Uncertainty b_{WM}	Systematic Uncertainty b_{GT}
Weak magnetism	b_{WM}	43.4	1.2 [11]	N/A	0.0034
Induced tensor form factor	d	40.5	3.7 [11]	0.2	0.0004
Fermi matrix element	c_{1h}	0.253	0.004 [11]	0.5	0.0017
Second forbidden matrix element	c_{2h}	0.755 fm^2	0.257 fm^2 [12]	0.2	0.0011

8.6 Preliminary Results

The preliminary result of the measurement of the weak magnetism form factor is $b_{WM} = 41.0 \pm 1.9_{\text{stat}} \pm 3.2_{\text{sys}}$. The preliminary result of the measurement of the Fierz term is $b_{GT} = 0.0021 \pm 0.0051_{\text{stat}} \pm 0.0084_{\text{sys}}$. The statistical uncertainty is with 7×10^6 events that pass the gamma coincidence with the data. Since this is a preliminary result, it is not yet

compared here to previous measurements.

Chapter 9

Conclusion

The half-life in ^{20}F has been measured to be $11.0011 \pm 0.0069_{\text{stat}} \pm 0.0030_{\text{sys}}$ s. This result has been published and is the most precise measurement of the half-life of ^{20}F to date. A preliminary result of the Fierz term has been obtained and is $0.0021 \pm 0.0051_{\text{stat}} \pm 0.0084_{\text{sys}}$. Using equation 1.8, the constraint on the underlying tensor coupling constant is $Re(\epsilon_T) = 0.00034 \pm 0.00082_{\text{stat}} \pm 0.00136_{\text{sys}}$. This assumes that the only new physics beyond the standard model is the tensor coupling.

9.1 Outlook

This analysis is not yet complete. To complete the analysis, first several systematic effects have to be added and reevaluated. The relative normalization of the beta-gamma sum spectrum is one of them. The energy deposited in the gamma can be similarly split into two parts. Then, by fitting the gamma spectra with the relative normalization as a free parameter, the value and uncertainty can be determined more accurately. This will likely reduce the uncertainty due to this effect. Another method would be to compare the output of GEANT4 to that of another simulation code. EGSnrc is being used by the collaborators from Wittenberg University.

Two systematic effects still have to be evaluated. Both deal with the inputs of the GEANT4 Monte Carlo. The first is the uncertainty due to different physics lists. This will

require running GEANT4 again. The second uncertainty has to do with an uncertainty due to the detector geometry. The detector geometry will have to be varied by some amount, and GEANT4 run again.

9.1.1 Possible Improvements of the Technique

For future experiments, other improvements of this technique could be done. Ideally, the lowest lower beta cut should be used for the fit. This both increases the statistics in the spectrum and decreases the uncertainty due to the uncertainty in b_{WM}. Going below 200 keV for this measurement is not possible due to the non-linearities in the detector. If the issue with the shape of the PVT detector spectrum could be solved, the spectrum could be measured down to smaller energies, since plastic detectors are linear down to about 125 keV [43].

In order to increase the efficiency for the 1.6 MeV gamma ray, the implant detector could be more completely encased with gamma detectors. If these gamma detectors had a higher resolution, that would decrease the background in the gamma windows. If that were coupled with a plastic detector, which would reduce the amount of bremsstrahlung, and a much cleaner spectrum would be measured.

To decrease the uncertainty on the extracted value of b_{WM}, a new and more precise measurement of the width of the isobaric analogue state in ^{20}Ne would have to be performed. This is the parameter Γ_{M1} in equation 3.29. This is the parameter that dominates the uncertainty in the calculation of b_{WM} [11]. This would allow for a more precise measurement of b_{GT} in ^{20}F to be made.

This calorimetric technique could be used for other allowed Gamow-Teller transitions. These other transitions would need to have a more precisely know b_{WM} value. Those with

higher maximum energies would need an accelerator powerful enough to implant the beam deep enough to absorb all the electron energy. A nucleus with a lower maximum electron energy, such as ^{6}He, would be more sensitive to the $1/E$ dependence of the Fierz term. This technique is a promising method for precision measurements in nuclear beta decay.

BIBLIOGRAPHY

BIBLIOGRAPHY

[1] J. D. Jackson, S. B. Treiman, and H. W. Wyld. Possible tests of time reversal invariance in beta decay. *Phys. Rev.*, 106:517–521, May 1957.

[2] T. D. Lee and C. N. Yang. Question of parity conservation in weak interactions. *Phys. Rev.*, 104:254–258, Oct 1956.

[3] J. C. Hardy and I. S. Towner. Superallowed $0^+ \to 0^+$ nuclear β decays: 2014 critical survey, with precise results for V_{ud} and ckm unitarity. *Phys. Rev. C*, 91:025501, Feb 2015.

[4] K. P. Hickerson, X. Sun, Y. Bagdasarova, D. Bravo-Berguño, L. J. Broussard, M. A.-P. Brown, R. Carr, S. Currie, X. Ding, B. W. Filippone, A. García, P. Geltenbort, J. Hoagland, A. T. Holley, R. Hong, T. M. Ito, A. Knecht, C.-Y. Liu, J. L. Liu, M. Makela, R. R. Mammei, J. W. Martin, D. Melconian, M. P. Mendenhall, S. D. Moore, C. L. Morris, R. W. Pattie, A. Pérez Galván, R. Picker, M. L. Pitt, B. Plaster, J. C. Ramsey, R. Rios, A. Saunders, S. J. Seestrom, E. I. Sharapov, W. E. Sondheim, E. Tatar, R. B. Vogelaar, B. VornDick, C. Wrede, A. R. Young, and B. A. Zeck. First direct constraints on fierz interference in free-neutron β decay. *Phys. Rev. C*, 96:042501, Oct 2017.

[5] M. González-Alonso, O. Naviliat-Cuncic, and N. Severijns. New physics searches in nuclear and neutron β decay. *Progress in Particle and Nuclear Physics*, 104:165 – 223, 2019.

[6] Oscar Naviliat-Cuncic and Martín González-Alonso. Prospects for precision measurements in nuclear decay in the lhc era. *Annalen der Physik*, 525(8-9):600–619, 2013.

[7] Adam Falkowski, Martín González-Alonso, and Kin Mimouni. Compilation of low-energy constraints on 4-fermion operators in the smeft. *Journal of High Energy Physics*, 2017, 06 2017.

[8] D. H. Wilkinson and D. E. Alburger. Mirror symmetry in the β decay of the $a = 20$ and 25 systems. *Phys. Rev. Lett.*, 24:1134–1136, May 1970.

[9] D. E. Alburger and F. P. Calaprice. Half-lives of ^{18}Ne and ^{20}F. *Phys. Rev. C*, 12:1690–1691, Nov 1975.

[10] Steven Weinberg. Charge symmetry of weak interactions. *Phys. Rev.*, 112:1375–1379, Nov 1958.

[11] K. Minamisono, T. Nagatomo, K. Matsuta, C. D. P. Levy, Y. Tagishi, M. Ogura, M. Yamaguchi, H. Ota, J. A. Behr, K. P. Jackson, A. Ozawa, M. Fukuda, T. Sumikama, H. Fujiwara, T. Iwakoshi, R. Matsumiya, M. Mihara, A. Chiba, Y. Hashizume, T. Yasuno, and T. Minamisono. Low-energy test of second-class current in β decays of spin-aligned ^{20}f and ^{20}na. *Phys. Rev. C*, 84:055501, Nov 2011.

[12] L. Van Elmbt, J. Deutsch, and R. Prieels. Measurement of the 20f beta-spectrum: A low-energy test of the standard electro-weak gauge-model. *Nuclear Physics A*, 469(3):531 – 556, 1987.

[13] D.W. Hetherington, A. Alousi, and R.B. Moore. The shape factor of the 20f beta spectrum. *Nuclear Physics A*, 494(1):1 – 35, 1989.

[14] Meng Wang, G. Audi, F. G. Kondev, W.J. Huang, S. Naimi, and Xing Xu. The AME2016 atomic mass evaluation (II). tables, graphs and references. *Chinese Physics C*, 41(3):030003, mar 2017.

[15] D.R. Tilley, C.M. Cheves, J.H. Kelley, S. Raman, and H.R. Weller. Energy levels of light nuclei, a = 20. *Nuclear Physics A*, 636(3):249 – 364, 1998.

[16] Barry R. Holstein. Recoil effects in allowed beta decay: The elementary particle approach. *Rev. Mod. Phys.*, 46:789–814, 1974.

[17] I. Angeli and K. P. Marinova. Table of experimental nuclear ground state charge radii: An update. *Atomic Data and Nuclear Data Tables*, 99:69–95, January 2013.

[18] D.H. Wilkinson. Evaluation of beta-decay: I. the traditional phase space factors. *Nuclear Instruments and Methods in Physics Research Section A: Accelerators, Spectrometers, Detectors and Associated Equipment*, 275(2):378 – 386, 1989.

[19] Wolfgang Bühring. The screening correction to the fermi function of nuclear β-decay and its model dependence. *Nuclear Physics A*, 430(1):1 – 20, 1984.

[20] D.H. Wilkinson. Evaluation of beta-decay: Ii. finite mass and size effects. *Nuclear Instruments and Methods in Physics Research Section A: Accelerators, Spectrometers, Detectors and Associated Equipment*, 290(2):509 – 515, 1990.

[21] S. A. Fayans. Radiative Corrections and Recoil Effects in the Reaction $\bar{\nu}_e + P \to N + e^+$ at Low-energies. (In Russian). *Sov. J. Nucl. Phys.*, 42:590, 1985. [Yad. Fiz.42,929(1985)].

[22] Frank P. Calaprice, W. Chung, and B. H. Wildenthal. Calculation of recoil-order matrix elements for the beta decays of ^{20}F and ^{20}Na. *Phys. Rev. C*, 15:2178–2186, Jun 1977.

[23] A. Sirlin. General properties of the electromagnetic corrections to the beta decay of a physical nucleon. *Phys. Rev.*, 164:1767–1775, Dec 1967.

[24] D.H. Wilkinson. Evaluation of beta-decay part v. the z-independent outer radiative corrections for allowed decay. *Nuclear Instruments and Methods in Physics Research Section A: Accelerators, Spectrometers, Detectors and Associated Equipment*, 365(2):497 – 507, 1995.

[25] J.K. Knipp and G.E. Uhlenbeck. Emission of gamma radiation during the beta decay of nuclei. *Physica*, 3(6):425 – 439, 1936.

[26] William J. Byatt. Analytical representation of hartree potentials and electron scattering. *Phys. Rev.*, 104:1298–1300, Dec 1956.

[27] Murray Gell-Mann. Test of the nature of the vector interaction in β decay. *Phys. Rev.*, 111:362–365, Jul 1958.

[28] X. Huyan, O. Naviliat-Cuncic, P. Voytas, S. Chandavar, M. Hughes, K. Minamisono, and S.V. Paulauskas. Geant4 simulations of the absorption of photons in csi and nai produced by electrons with energies up to 4 mev and their application to precision measurements of the β-energy spectrum with a calorimetric technique. *Nuclear Instruments and Methods in Physics Research Section A: Accelerators, Spectrometers, Detectors and Associated Equipment*, 879:134 – 140, 2018.

[29] D. Weisshaar, A. Gade, T. Glasmacher, G.F. Grinyer, D. Bazin, P. Adrich, T. Baugher, J.M. Cook, C.Aa. Diget, S. McDaniel, A. Ratkiewicz, K.P. Siwek, and K.A. Walsh. Ceasar: A high-efficiency csi(na) scintillator array for in-beam gamma ray spectroscopy with fast rare-isotope beams. *Nuclear Instruments and Methods in Physics Research Section A: Accelerators, Spectrometers, Detectors and Associated Equipment*, 624(3):615 – 623, 2010.

[30] H. Tan, M. Momayezi, A. Fallu-Labruyere, Y. Chu, and W. K. Warburton. A fast digital filter algorithm for gamma-ray spectroscopy of double-exponential decaying scintillators. In *2003 IEEE Nuclear Science Symposium. Conference Record (IEEE Cat. No.03CH37515)*, volume 2, pages 784–788 Vol.2, Oct 2003.

[31] Ron Fox. Nscl data acquisition documentation, 2017.

[32] M. Hughes, E. A. George, O. Naviliat-Cuncic, P. A. Voytas, S. Chandavar, A. Gade, X. Huyan, S. N. Liddick, K. Minamisono, S. V. Paulauskas, and D. Weisshaar. Measurement of the ^{20}F half-life. *Phys. Rev. C*, 97:054328, May 2018.

[33] S Malmskog and J Konijn. Half-life measurements of 6he, 16n, 19o, 26f, 28al, 77senm and 110ag. *Nuclear Physics*, 38:196 – 210, 1962.

[34] S. S. Glickstein and R. G. Winter. Properties of f^{20}. *Phys. Rev.*, 129:1281–1283, Feb 1963.

[35] Herbert P. Yule. Half-lives of some short-lived radioactive isotopes. *Nuclear Physics A*, 94(2):442 – 448, 1967.

[36] H. Genz, A. Richter, B.M. Schmitz, and H. Behrens. Half-life, endpoint energy, ft value and shape factor in the β- decay of 20f. *Nuclear Physics A*, 267:13 – 28, 1976.

[37] Tadanori Minamisono. Nmr of short-lived nuclei implanted in crystals and a new isol for projectile fragments in relativistic heavy-ion reaction. *Hyperfine Interactions*, 35(1):979–991, Apr 1987.

[38] T.F. Wang, R.N. Boyd, G.J. Mathews, M.L. Roberts, K.E. Sale, M.M. Farrell, M.S. Islam, and G.W. Kolnicki. Measurement of the half-life of 20f. *Nuclear Physics A*, 536(1):159 – 167, 1992.

[39] S. Itoh, M. Yasuda, H. Yamamoto, T. Iida, A. Takahashi, and K. Kawade. Measurement of Beta-decay Half-lives of Short-lived Nuclei by Using High-rate Spectroscopy Amplifier. In *1994 Symposium on Nuclear Data*, Tokai, Japan, March 1995.

[40] D. P. Burdette, M. Brodeur, T. Ahn, J. Allen, D. W. Bardayan, F. D. Becchetti, D. Blankstein, G. Brown, B. Frentz, M. R. Hall, S. King, J. J. Kolata, J. Long, K. T. Macon, A. Nelson, P. D. O'Malley, C. Seymour, M. Skulski, S. Y. Strauss, and A. A. Valverde. Resolving the discrepancy in the half-life of ^{20}F. *Phys. Rev. C*, 99:015501, Jan 2019.

[41] S. Agostinelli, J. Allison, K. Amako, J. Apostolakis, H. Araujo, P. Arce, M. Asai, D. Axen, S. Banerjee, G. Barrand, F. Behner, L. Bellagamba, J. Boudreau, L. Broglia, A. Brunengo, H. Burkhardt, S. Chauvie, J. Chuma, R. Chytracek, G. Cooperman, G. Cosmo, P. Degtyarenko, A. Dell'Acqua, G. Depaola, D. Dietrich, R. Enami, A. Feliciello, C. Ferguson, H. Fesefeldt, G. Folger, F. Foppiano, A. Forti, S. Garelli, S. Giani, R. Giannitrapani, D. Gibin, J.J. Gómez Cadenas, I. González, G. Gracia Abril, G. Greeniaus, W. Greiner, V. Grichine, A. Grossheim, S. Guatelli, P. Gumplinger, R. Hamatsu, K. Hashimoto, H. Hasui, A. Heikkinen, A. Howard, V. Ivanchenko, A. Johnson, F.W. Jones, J. Kallenbach, N. Kanaya, M. Kawabata, Y. Kawabata, M. Kawaguti, S. Kelner, P. Kent, A. Kimura, T. Kodama, R. Kokoulin, M. Kossov, H. Kurashige, E. Lamanna, T. Lampén, V. Lara, V. Lefebure, F. Lei, M. Liendl, W. Lockman, F. Longo, S. Magni, M. Maire, E. Medernach, K. Minamimoto, P. Mora de Freitas, Y. Morita, K. Murakami, M. Nagamatu, R. Nartallo, P. Nieminen, T. Nishimura, K. Ohtsubo, M. Okamura, S. O'Neale, Y. Oohata, K. Paech, J. Perl, A. Pfeiffer, M.G. Pia, F. Ranjard, A. Rybin, S. Sadilov, E. Di Salvo, G. Santin, T. Sasaki, N. Savvas, Y. Sawada, S. Scherer, S. Sei, V. Sirotenko, D. Smith, N. Starkov, H. Stoecker, J. Sulkimo, M. Takahata, S. Tanaka, E. Tcherniaev, E. Safai Tehrani, M. Tropeano, P. Truscott, H. Uno, L. Urban, P. Urban, M. Verderi, A. Walkden, W. Wander, H. Weber, J.P. Wellisch, T. Wenaus, D.C. Williams, D. Wright, T. Yamada, H. Yoshida, and D. Zschiesche. Geant4—a simulation toolkit. *Nuclear Instruments and Methods in Physics Research Section A: Accelerators, Spectrometers, Detectors and Associated Equipment*, 506(3):250 – 303, 2003.

[42] John von Neumann. Various techniques used in connection with random digits. pages 36–38, 1951.

[43] Glenn F Knoll. *Radiation detection and measurement; 4th ed.* Wiley, New York, NY, 2010.